Studies of Magnetic Logic Devices

by

Likun Hu

A thesis
presented to the University of Waterloo
in fulfillment of the
thesis requirement for the degree of
Master of Applied Science
in
Electrical and Computer Engineering

Waterloo, Ontario, Canada, 2012

I hereby declare that I am the sole author of this thesis. This is a true copy of the thesis, including any required final revisions, as accepted by my examiners.

I understand that my thesis may be made electronically available to the public.

Abstract

Magnetic nanoscale devices have shown great promise in both research and industry. Magnetic nanostructures have potential for non-volatile data storage applications, reconfigurable logic devices, biomedical devices and many more.

The S-state magnetic element is one of the promising structures for non-volatile data storage applications and reconfigurable logic devices. It is a single-layer logic element that can be integrated in magnetoresistive structures. We present a detailed micromagnetic analysis of the geometrical parameter space in which the logic operation is carried out. The influence of imperfections, such as sidewall roughness and roundness of the edge is investigated.

Magnetic nanowires are highly attractive materials that has potential for applications in ultrahigh magnetic recording, logic operation devices, and micromagnetic and spintronic sensors. To utilize applications, manipulation and assembly of nanowires into ordered structures is needed. Magnetic self-alignment is a facile technique for assembling nanowires into hierarchical structures. In my thesis, I focus on synthesizing and assembling nickel nanowires. The magnetic behaviour of a single nickel nanowire with 200 nm diameter is investigated in micromagnetic simulations. Nickel nanowires with Au caps at the ends were synthesized by electrochemical deposition into nanopores in alumina templates. One-dimensional alignment, which forms chains and two-dimensional alignment, which forms T-junctions as well as cross-junctions are demonstrated. Attempts to achieve three-dimensional alignment were not successful yet. I will discuss strategies to improve the alignment process.

Acknowledgements

First and foremost, I would like to sincerely express my gratitude to my supervisor, Professor Thorsten Hesjedal, for his support and guidance. Without his inspiration, precious advise and enormous patience, I would not be able to finish my graduate study in University of Waterloo. His attitude towards research, family and students inspired me to think differently about my work, study and life, and it will influence me for years to come. Without Professor Hesjedal's support and encouragement, I would not have been able to obtain the opportunity to study in this field and would not have been able to gain valuable industrial experiences. The entire graduate experience has been fantastic and unforgettable thanks to my supervisor.

I would like to acknowledge Professor Siva Sivoththaman for his help and support on my program completion.

I would alse like to thank kindly the members of our research group: Randy Fagan, James Mracek and Daniel Russo for their help with my research.

Finally, my deepest gratitude goes to my parents for their support and encouragement.

Contents

List of Tables

List of Figures

Chapter 1

Introduction

1.1 Motivation

The silicon microchip has been one of the most impressive pieces of engineering ever made. Moore's law introduced by Gordon Moore in 1965 describes a long term trend that the number of transistors that can be placed inexpensively on an integrated circuit that doubles approximately every two years [1]. This prediction has lasted for nearly 45 years. The capabilities of many digital electronic devices are strongly linked to Moore's Law: processing speed, memory capacity, sensors, etc.

At present, researchers are still trying to exploit the properties of semiconductors and production processes. Like all other technologies, however, it will stop growing exponentially and enter the realm of diminishment. In recent years, there is a clear trend that the performance scaling of uniprocessor is saturating, so we can no longer follow this doubling path [1]. Figure 1.1 shows the historic microprocessor clock frequency statistics [2]. This figure shows a clear trend that the speed of microprocessor is saturating. There are several possible barriers underlying semiconductor manufacturing for continuing density doubling. The gigabit chip generation, for example, may finally force technologists up against the

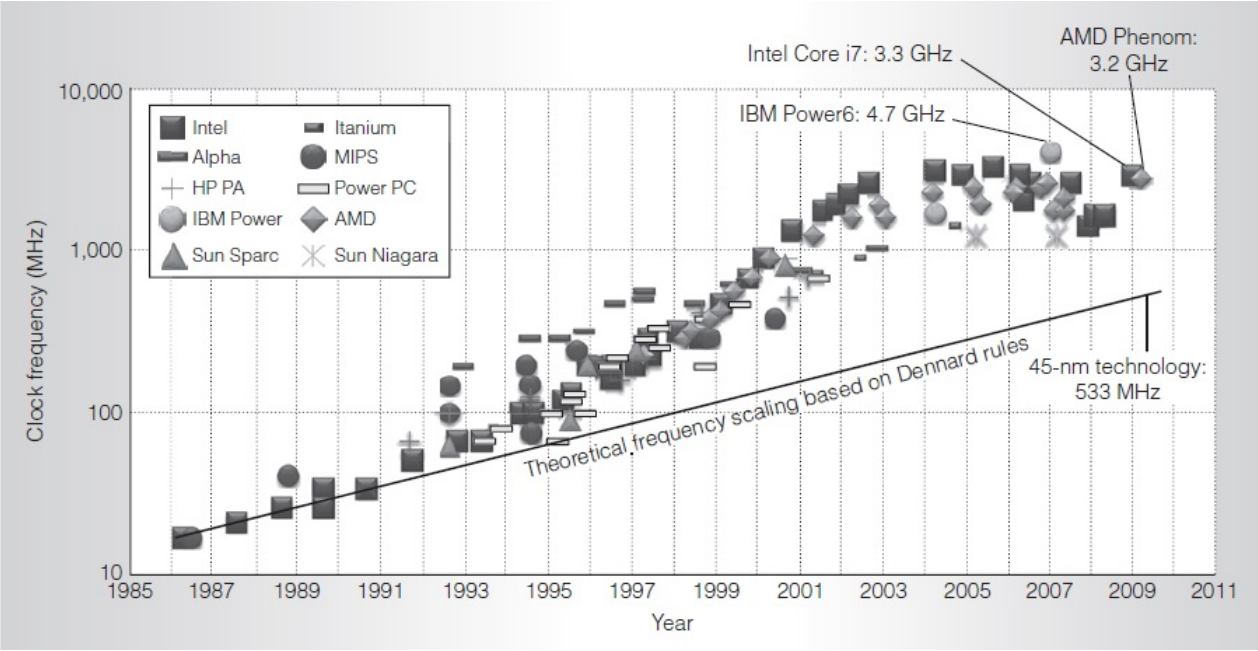

Figure 1.1: Historic microprocessor clock frequency statistics [2]. Power consumption has been increasing by about two orders of magnitude for last two decades. (PA is the abbreviation for Precision Architecture)

limits of optical lithography. At the same time, the cost will rise exponentially along with component densities, and it is possible that the price per transistor will bottom out, means that there will be no profit in making transistors smaller. In fact, economics may constrain Moore's Law before physics does [1].

1.2 Magnetic Logic Devices

Magnetic logic devices have been widely explored for memory and sensor applications. These devices make it possible to achieve programmable and nonvolatile logic functionalities [3]. Using ferromagnetic materials for logic operation is not a new idea, and it was commercialized over 60 years ago [4]. Ferromagnetic materials have also been considered

for applications of logic operation in digital computers since the appearance of the first magnetic memory device. Hans Gschwind summarized the reasons why magnetic logic devices are rather attractive to the computer designer [5]:

- They possess the nonvolatility of the stored information.
- They require in most applications no power other than the power to switch their states, which can greatly reduce power consumption.
- They have the potential to perform all required operations for computer at room temperature, i.e., full logic function, storage and amplification.

Magnetic logic devices are experiencing a comeback [3]. Programmable logic functions may be implemented as conventional programmed logic arrays that use the magnetic devices as the nonvolatile programming elements or as arrays of universal logic gates. So the core logic functions are magnetically programmed. The key feature of ferromagnetic components for logic operation is magnetic hysteresis, which describes the magnetization of the components as a function of external magnetizing force and magnetization history. Nearly all applications rely on particular aspects of hysteresis heavily [6].

Imre *et al.* [6] have experimentally demonstrated a universal logic gate based on magnetic structures. Its structure is based on the concept of cellular automata which are networks of cells with rules that describe how neighboring cells interact. Figure 1.2(a) shows the structure proposed by Imre. The magnetic state of nanomagnets "A", "B", and "C" can be set by some inputs; the majority logic operation will be performed by the central nanomagnet "M"; and the result can be transferred to the nanomagnet labelled as "out". The overall cross-geometry can be schematically represented by the symbol in Fig. 1.2(b) and the truth table is introduced in Tab. 1.2. The state of center nanomagnet "M" takes the majority state of its three inputs and the output nanomagnet "out" takes the inverted state. From the truth table, if one of the three inputs constantly tied to logic

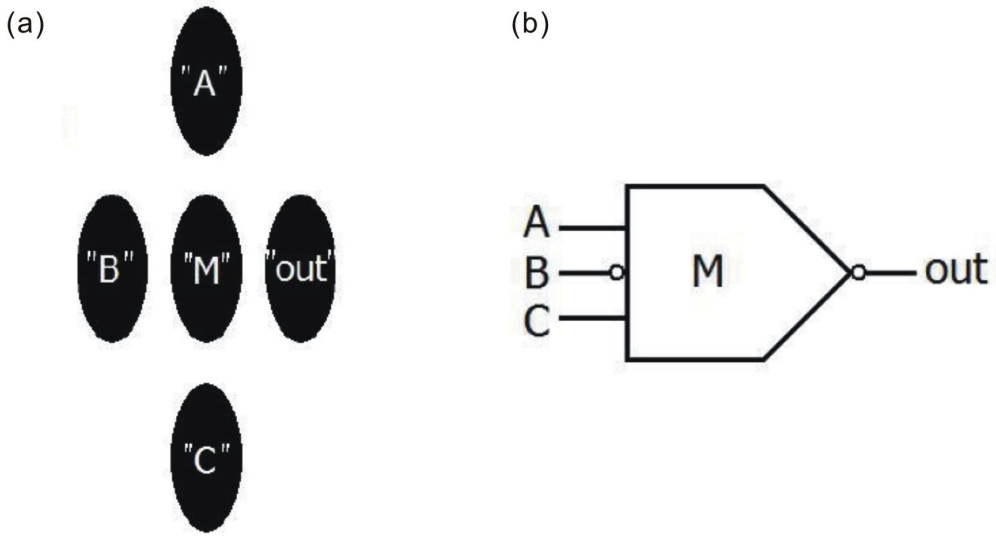

Figure 1.2: Magnetic majority gate. [7] (a) Majority gate geometry consists of elongated nanomagnets. (b) Majority gate symbol.

1, then the gate performs the NOR operation. On the contrary, if one of the three inputs tied permanently to logic 0, then the gate simply perform NAND operation. This single gate proposed by Imre can performs both NAND and NOR operations.

All other types of Boolean logic gates, i.e., AND, OR, NOT, XOR, XNOR, can be created from a suitable network of NAND gates, NOR gates, or the combination of the two. Due to this property, NAND and NOR gates are sometimes called "universal gates". The convenience of having a single universal gate gives the possibility of building programmable logic hardware. The word 'programmable' is used here to indicate that the actual function of the gate can be reconfigured after the hardware has been built. By enabling users to effectively create customized hardware, many different applications can be allowed in a single chip, which reduces both cost and time. The ability to reconfigure logic is useful for more than simple device prototyping [3].

A	B	C	A$\bar{B}$C	M	out
0	0	0	010	0	1
0	0	1	011	1	0
1	0	0	110	1	0
1	0	1	111	1	0
0	1	0	000	0	0
0	1	1	001	0	1
1	1	0	100	0	1
1	1	1	101	1	0

Table 1.1: Truth-table of the majority gate geometry

Another noteworthy feature of the magnetic majority gate is that it uses an adiabatic switch scheme. The adiabatic switch scheme makes the energy barriers between discrete data states gradually lowered and then raised again, which allows the system gradually move from one computational state to another without wasting the energy like the conventional architectures [8].

One of the challenges of magnetic logic device speed. For Imre's work, it is closely related to MRAM (magnetic random-access memory), where sub-nanosecond switching is commonplace by using the spin-torque transfer effect to rotate the magnetization instead of using magnetic fields, which operation reaches GHz [9]. This speed is still a magnitude slower than CMOS logic devices, so there would be little advantage in constructing an entire microprocessor from magnetic logic elements. The greatest challenge that magnetic logic devices are facing may be constructing applications where its strength can be mostly utilized. Many people believe that the future of microelectronics lies in a diverse hybrid of technologies on a single platform [10], like putting magnetic logic devices and CMOS logic devices together to make hybrid circuits.

1.3 Magnetic Nanowire Assemblies

Nanowires are highly attractive materials due to the critical structural characteristics, transportation properties and optical properties. The synthetic methods of nanowires are getting mature, and nanowires can be reproduced in the cost-effective ways [11], it is only a matter of time before applications will be intensively developed. As we know the semiconductor industry is approaching its limit where the physical barriers and economics factors will constrain its growing pace. These anticipated limits to future microelectronics have led to intense research towards substantial technologies and devices for digital logic operations. Since nanowires are comparable in size to shrinking electronic components, nanowires naturally become good candidates for specific applications in electronics [12, 13], optics [14], chemical and biology sensor [15], and magnetic media [16].

Magnetic nanowires hold very high potential for applications in ultra-high density magnetic recording [17], logic operation devices [18], and spintronic sensors [19]. Magnetic nanowires are quasi one-dimensional and can perform self-assembly with external magnetic fields. Self-assembly is the process of unifying a structure from the components acting under forces/motives internal or local to the components themselves, and raising through their interaction [20]. The self-assembly process can be used as a technique for bottom-up computational nanostructures like crossbar-based computing structure. Cross-junction and T-junction magnetic nanowire networks, which are demonstrated using sequential alignment technique [21], attract our attention. These assembled nano networks have the potential to construct crossbar-based computing structures [20]. Configurable crossbars that consist of two or more parallel planes of nanowires are the nanoscale computational structures. The crossbar-based nanoarchitectures can be classified into two distinct dimensional structure namely two-dimensional (2D) structures and three-dimensional (3D) structures [22].

Chapter 2

Micromagnetics

2.1 Introduction

The increasing importance of understanding the particular properties of magnetic micro- and nano-structures brings the discussion of micromagnetics. Micromagnetism is the continuum theory of magnetic moments, underlying the description of magnetic microstructure. The length scale that micromagnetics deals with is larger than lattice constant but small enough to resolve the internal structure of domain walls [23]. The micro- and nanostructures are small enough that quantum mechanical effects like the exchange interaction have to be taken into account, however, they exceed the capabilities of today's computational models for a pure quantum mechanical description. The theory of micromagnetics provides the mathematical framework to describe static and magnetization structures. A solution of the underlying equations can usually only be achieved with numerical methods.

2.2 Energy Contributions in Micromagnetics

We know the basic concept of micromagnetism is to replace the atomic magnetic moments by a continuous function of position. A continuous magnetization function $\mathbf{M}(\mathbf{r})$ is used to represent the locally averaged density of magnetic moments:

$$\mathbf{M}(\mathbf{r}) = \frac{1}{V(\mathbf{r}, \Delta r)} \sum_{i \in \mathbb{J}(\mathbf{r}, \Delta r)} \mu_{\mathbf{i}} \tag{2.1}$$

Here, $V(\mathbf{r}, \Delta r)$ is a sphere of radius Δr. $\mathbb{J}(\mathbf{r}, \Delta r)$ is the index of magnetic moments $\mu_{\mathbf{i}}$ in the volume $V(\mathbf{r}, \Delta r)$. The averaging can be carried out on the scale of exchange length that will contain many magnetic moments. In the micromagnetics concept, we assume $\mathbf{M}(\mathbf{r})$ is a continuous and differentiable function, the expression Equation 2.1 can be described using differential operators. The resulting function can be solved numerically.

The magnetization $\mathbf{m}(\mathbf{r})$ is an independent variable that will not be affected by the material size:

$$\mathbf{m}(\mathbf{r}) = \mathbf{M}(\mathbf{r})/M_s \tag{2.2}$$

Where M_s is the saturation magnetization of the material. So we have $|\mathbf{m}_s| = 1$, and the magnetization $\mathbf{m}(\mathbf{r})$ is under the constrain of $|\mathbf{m}| < 1$.

2.2.1 Exchange Energy

In 1928, Heisenberg showed that a Weiss "molecular field" can be explained using a quantum mechanical treatment of the many-body problem [24]. A term of electrostatic origin in the energy of interaction between neighbouring atoms that tends to align the electron spins parallel to each other is called exchange integral, and it doesn't have a classical

analog [25]. The exchange interaction can be explained by the Pauli exclusion principle. If two electrons in an atom have anti-parallel spins, then they will be able to share one atomic or molecular orbital. So the two electrons will overlap spatially, thus increasing the electrostatic Coulomb repulsion. On the other hand, if two electrons have parallel spins, then they will have to occupy two different orbitals and will have less Coulomb repulsion. The orientation of electron spins thus determines the electrostatic Coulomb interaction between the electrons [25].

In classical approximation, the exchange energy between two moments can be given by the Heisenberg Hamiltonian, and the sum of all the exchange energy will give the total exchange energy:

$$\epsilon_{ex} = -2\sum_{i<j} J_{ij}\mathbf{S}_i \cdot \mathbf{S}_j = -2S^2 \sum_{i<j} J_{ij}\cos\phi_{ij} \tag{2.3}$$

Where $\mathbf{S}$ is the unit vector of the direction of one magnetic moment. J_{ij} represents the constant in exchange integral of interacting spins $\mathbf{S}_i$ and $\mathbf{S}_j$ at the location $\mathbf{r}_i$ and $\mathbf{r}_j$. Here, ϕ_{ij} represents the angle between interacting spins $\mathbf{S}_i$ and $\mathbf{S}_j$.

Equation 2.3 is a classical approximation. Its transition to micromagnetics is to replace the spin operators by the continuous functions of $\mathbf{m}(\mathbf{r})$ which is the averaged magnetic moment at its respective position. ϕ_{ij} is assumed to be small. An approximation can be applied as:

$$\cos\phi_{ij} \approx 1 - 1/2\phi_{ij}^2 \tag{2.4}$$

Since $\mathbf{S}_i$ is a unit vector, which$|\mathbf{S}_i| = |\mathbf{S}_j| = 1$. Another approximation can be made here [26]:

$$\begin{aligned} |\phi_{i,j}| &\approx |\mathbf{S}_i - \mathbf{S}_j| \\ &= a\frac{|\mathbf{S}_i - \mathbf{S}_j|}{a} \end{aligned} \tag{2.5}$$

where a represents the lattice spacing and $\frac{|\mathbf{S}_i - \mathbf{S}_j|}{a}$ therefore can approximate the spatial derivation of $\mathbf{S}$ over lattice spacing a. Take $\mathbf{r}_{i,j}$ to be a lattice translation vector, and then

we have

$$|\mathbf{S}_i - \mathbf{S}_j| = \nabla_{\mathbf{r}_{i,j}} \mathbf{S} \tag{2.6}$$

Put it back into Equation 2.3, it will be [27]:

$$\begin{aligned} \epsilon_{ex} &= -JS^2 \sum_i \sum_{j \neq i}^{N} [(\mathbf{r}_{i,j} \cdot \Delta)\mathbf{S}]^2 \\ &= -JS^2 \sum_i \sum_{j \neq i}^{N} [(\Delta m_x)^2 + (\Delta m_y)^2 + (\Delta m_z)^2] \end{aligned} \tag{2.7}$$

Now ignore the discrete lattice and obtain the continuous form:

$$\epsilon_{ex} = A \int_V [(\nabla S_x)^2 + (\nabla S_y)^2 + (\nabla S_z)^2] d^3 r \tag{2.8}$$

where $A = \frac{JS^2 z}{a}$ is the exchange stiffness tensor, which is temperature dependent in general. The exchange tensor A is defined to be positive to make sure an energy increase with a change in the magnetization. It is typically assumed to be isotropic.

2.2.2 Anisotropy Energy

Anisotropy energy depends on the direction of the magnetization relative to the structural axes of the material. This dependence results in the spin-orbital interactions that couples the spin moment to the lattice.

An expansion of the power series of magnetization components that is relative to the crystal axes can show the important contributes. Typically, the first two significant terms need to be considered because the thermal agitation of the spin tends to average out the contributions of the higher-order terms. Significant higher-order terms have been observed only at low temperatures [23]. The basic formula for the anisotropy energy density of a cubic crystal is:

$$e_{Kc} = K_{c1}(m_1^2 m_2^2 + m_1^2 m_3^2 + m_2^2 m_3^2) + K_{c2} m_1^2 m_2^2 m_3^2 \tag{2.9}$$

where the m_i are the magnetization components along the cubic axes. K_{c1} and K_{c2} are the effective anisotropy constants. Mostly, K_{c2} and higher-order terms can be neglected.

The material, NiFe, used in this work is polycrystalline and ferromagnetically soft, so the magnetocrystalline anisotropy energy will be neglected in later simulations.

2.2.3 Zeeman Energy

Zeeman energy is also called external field energy. It is an energy term that represents the interaction energy of the magnetization vector field with an external field $\mathbf{H}_{ext}$. The zeeman energy can be given by:

$$E_{ext} = -\mu_0 \int \mathbf{H}_0 \cdot \mathbf{M} dr^3 \tag{2.10}$$

where $\mathbf{M}$ is the local magnetization. When the magnetization $\mathbf{M}$ is aligned parallel to the external magnetic field, then the Zeeman energy is minimized.

2.2.4 Stray Field Energy

The stray field originates from the magnetization vector field itself. It is also called demagnetization field, which has the tendency of acting on the magnetization so as to reduce the total magnetic moment. The energy connected to the stray field is [23]:

$$E_d = \frac{\mu_0}{2} \int_{all\ space} \mathbf{H}_d^2(\mathbf{r}) dV = -\frac{\mu_0}{2} \int_{sample} \mathbf{M}(\mathbf{r}) \cdot \mathbf{H}_d(\mathbf{r}) dV \tag{2.11}$$

where $\mathbf{H}_d$ is defined as stray field. The first integral is for all space. The stray field is difficult to analytically solve, with exception of some simple shapes, such as an ellipsoid. The demagnetization energy will always be positive except for the case where the stray field is zero everywhere. The second integral extends over the magnetic material which is more practical to numerically calculate.

2.3 Micromagnetic Equations

The micromagnetic equations are non-linear and non-local, which are difficult to solve analytically in most of the cases. Because of the increasing need of understanding for particular properties of magnetic micorstructures and nanostructures, numerical solutions are increasingly pursued. The mathematical approach of micromagnetism started with the introduction of the Landau-Lifshitz free energy. Micromagnetic theory considers the total free energy in the ferromagnetic materials: [23, 25]

$$E_{\text{tot}} = E_{\text{ex}} + E_{\text{ani}} + E_{\text{d}} + E_{\text{ext}} + E_{\text{ext.stress}} + E_{\text{e}} \tag{2.12}$$

It includes contributions such as the exchange energy E_{ex}, the magnetocrystalline anisotropy energy E_{ani}, the stray field energy E_{d}, the external field energy (Zeeman Energy) E_{ext}, the external stress energy $E_{\text{ext.stress}}$, as well as the magnetostrictive self-energy E_{e}.

At equilibrium state, the total free energy is minimized with respect to the magnetization $\mathbf{m}(\mathbf{r})$. The micromagnetic equations of equilibrium state of the system can be obtained by using the variational calculus introduced by Brown [28]:

$$\frac{\partial E_{\text{tot}}}{\partial \mathbf{m}(\mathbf{r})} = 0 \tag{2.13}$$

where E_{tot} is the total free energy and $\mathbf{m}(\mathbf{r})$ is the magnetization. Here we take Brown's equations to calculate energy and the effective field $\mathbf{H}_{\text{eff}}$ [28]:

$$E_{\text{tot}} \quad = \quad -\int \mu_0 \mathbf{H}_{\text{eff}}(\mathbf{r}) \cdot \mathbf{M}(\mathbf{r}) d^3 r \tag{2.14}$$

where

$$\mathbf{H}_{\text{eff}} = -\frac{1}{\mu_0} \frac{\partial E_{\text{tot}}}{\partial \mathbf{M}(\mathbf{r})} \tag{2.15}$$

The dynamics of the magnetization is due to a torque. The equation of motion for describing the time evolution of the magnetization in a magnetic field is given by the Landau-

Lifshitz-Gilbert equation [29]:

$$\frac{\partial \mathbf{M}(\mathbf{r},t)}{\partial t} = -\frac{\gamma}{1+\alpha^2}\mathbf{M}(\mathbf{r},t) \times \mathbf{H}_{\text{eff}}(\mathbf{r},t) \\ -\frac{\alpha\gamma}{(1+\alpha^2)\cdot M_s}\mathbf{M}(\mathbf{r},t) \times [\mathbf{M}(\mathbf{r},t) \times \mathbf{H}_{\text{eff}}(\mathbf{r},t)] \tag{2.16}$$

where $\mathbf{H}_{\text{eff}}$ is the effective magnetic field; γ is the electron gyromagnetic ratio; and α is a phenomenological damping constant which is usually between 0.1 to 1. This equation calculates the path through the energy landscape, starting from the initial magnetization and moving towards the energy minimum. The first term of the right-hand side of Eq. 2.16 illustrated in Fig.2.1 (a) describes the gyromagnetic precession of the magnetization around the effective field. The second term is a viscous damping term that rotates the magnetic polarization vector parallel to the field. The influence of the damping parameter on magnetization dynamics is shown in Fig. 2.1 (b). The Landau-Lifshitz-Gilbert equation is the most widely used approach in micromagnetic simulations to find the equilibrium magnetization distribution. It is also the starting point of dynamic description of micromagnetic processes.

2.4 Micromagnetic Simulations

On this intermediate level, micromagnetic simulations have proven to be very useful to derive and explain the magnetization distribution and the dynamics of a ferromagnetic material.

By combining the classic micromagnetic theory with dynamic descriptions of magnetization orientations, micromagnetic simulations can predict complex magnetic domain configurations in ferromagnetic systems, the measurements of the remanent magnetization and the coercive field. Micromagnetic simulations have enriched our understanding of magnetic materials and successfully predicted the magnetic properties of some structures [31].

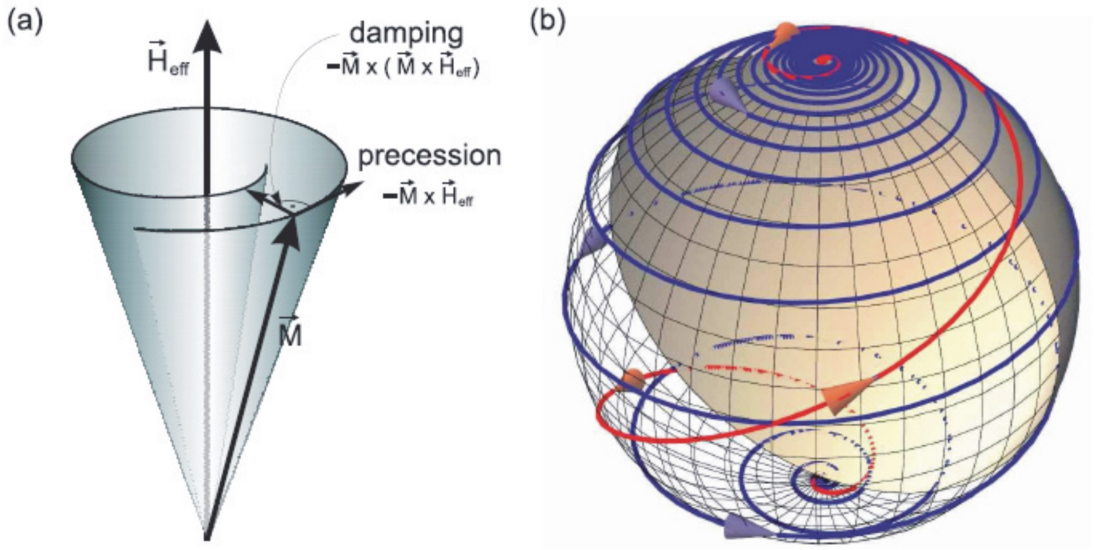

Figure 2.1: (a) Sketch of the gyromagnetic precession motion. (b) Calculated trajectories of a normalized magnetic moment on the unit sphere for two different damping parameters ($\alpha = 0.5$ red curve and $\alpha = 0.1$ blue curve). (a) and (b) are from [30].

To numerically find approximate solutions of partial differential equation (Eq. 2.16), the finite element method (FEM) and the finite difference method (FDM) are two commonly used techniques. These two approaches have been successfully applied in various fields of computer-aided engineering like structural analysis, fluid dynamics, electromagnetic field computation, as well as micromagnetics. The main differences between FEM and FDM are [32]:

- FDM will simply change the partial differential equation into a different equation. FEM will solve partial differential equations by solving an equivalent variation problem.

- FDM meshes the geometry with rectangular grids while FEM can handle all basic elements. FEM can handle complicated geometries and boundaries with relative ease while FDM, in its basic form, is restricted to handle rectangular shapes and simple

alterations.

- FDM can be easier implemented.
- The quality of a FEM approximation is often higher than in corresponding FDM approach but quality of a simulation is extremely problem-dependent.

2.5 Micromagnetic Simulators

A micromagnetic simulator is a computer program carrying out micromagnetic simulations. Micromagnetic simulators provide great freedom in the choice of experimental conditions and material parameters, such as object geometry, initial magnetization, time evolution of the external magnetic field, anisotropy, demagnetization factors, and the exchange interaction.

There are various commercial and free software packages available for micromagnetic modeling and simulations. There are some highly successful packages such as OOMMF, Magpar and LLG.

OOMMF, the Object-Oriented Micromagnetic Framework, is a free micromagnetic simulation tool using finite difference lattice discretisations of space and fast fourier transformation (FFT). It is a project of the Mathematical and Computational Sciences Division of Information Technology Laboratory (ITL) at National Institute of Standards and Technology (NIST), developed mainly by Mike Donahue and Don Porter, and distributed freely on the internet. It works user-friendly on a wide range of platforms.

Magpar is also an open source software package. It uses the finite element method for calculation that gives large flexibility in modelling arbitrary geometries.

LLG micromagnetic simulator was developed in 1997 by Michael R. Scheinfein. It is a widely used commercial software package using FDM.

Due to the uncertainty in the material parameters, the inaccurate experimental geometry, and the lack of material inhomogeneities, it is not reasonable to reproduce the experimental curve quantitatively or reproduce the actual domain structure exactly [33]. I would like to focus on the experimentally observed results in a qualitative way, independent of the exact simulation parameters [33]. By comparing imaging results and simulation results, people gain a lot of understanding on magnetic properties of some applications on sub-micron length scale.

2.6 Micromagnetic Systems

2.6.1 Hysteresis Loops

In a magnetic system, the plot of magnetization M versus magnetic field H is called the M-H hysteresis loop. Here, we use M/M_S instead of M which has values of 1 or -1 at saturations. The ferro- and ferrimagnets show an interesting behaviour when the magnetic field is reduced to zero and is reversed. A schematic plot of generic hysteresis loop is shown in Fig. 2.2. It starts at the origin in an unmagnetized state, and then the curve goes to saturation as an applied external positive magnetic field gradually increases. Then let the magnetic field H reduce to zero from saturation, while the magnetization value M/M_S correspondingly decreases from saturation to the remanent magnetization M_R/M_S. A reversed field which is required to reduce magnetization to zero is called coercive field, H_c. Depending on the value of the coercive field, the ferromagnetic material can be classified as either hard or soft [25]. When the external magnetic field continues decreasing, saturation will be achieved in the reversed direction.

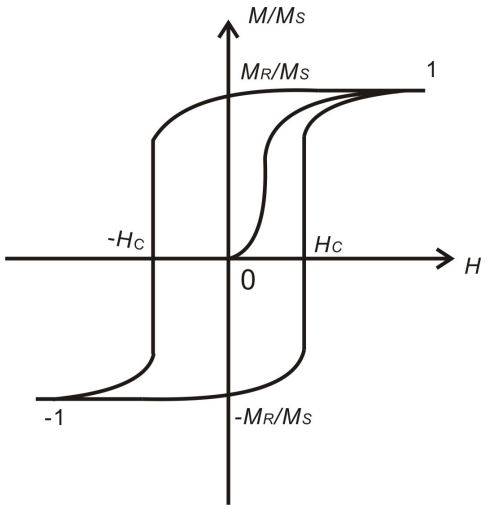

Figure 2.2: Schematic plot of hysteresis loop.

2.6.2 Ferromagnetic Domains

Domains are small regions in ferromagnetic materials in which all the magnetic moments are parallel to each other. The individual magnetic moments of the atoms are aligned with one another and they point in the same direction. Domains can be thought of as the magnetic structures that form at small scales within magnets in particular circumstances [23]. The formation of domains allows the material to minimize its total energy. The domain formation has numbers of contributions, like exchange energy, magnetocrystalline anisotropy energy, and magnetostatic energy. The magnetocrystalline anisotropy energy and magnetostrictive energy can influence the shape and size of domains [25]. The exchange energy that tends to align the magnetic moments provides a strong driving force for parallel alignment, while magnetostatic energy is the major driving force for domain formation.

A magnetized block of ferromagnetic material with a single domain has a macroscopic magnetization and behaves as a magnet with a magnetic field around it [25]. The stray field around the ferromagnetic block, so called demagnetization field, acts to magnetize

the block in opposite direction from its own magnetization. Domain formation will reduce the external demagnetization field which causes reducing magnetostatic energy. At the same time, more magnetic moments are not able to align parallel, so the exchange energy increases with domain formation. The battle between exchange energy and magnetostatic energy determines domain formation.

Magnetocrystalline and magnetostrictive energies influence the shape and size of domains. In ferromagnetic crystals, the magnetization tends to align along certain preferred crystalline directions, so called easy axis. It is easiest to magnetize the demagnetized ferromagnetic block if the external magnetic field is applied along the easy axis. This causes the magnetization to align itself along a preferred crystallographic direction. To minimize the magnetocrystalline energy, the magnetization should point along the easy axis. Magnetocrystalline energy clearly affects the structures of the domain boundaries. At the region between two adjacent domains, the magnetic moments cannot align along the easy axis, so, like exchange energy, the magnetocrystalline energy prefers large domains [25]. When a ferromagnet material is magnetized, it experiences a change in length, which is known as its magnetostriction. Nickel is a material that shrinks along the direction of magnetization and is said to have a negative magnetostriction. The length change is only tens of parts per million but still affects the domain structure. The magnetostriction energy can be lowered by reducing the size of the primary domains.

Chapter 3

Micromagnetic Investigation of the S-State Reconfigurable Logic Element

This chapter first introduces the S-state reconfigurable logic element. To establish a stable geometrical stability criteria, a detailed analysis of the geometrical dimensions and shape of the S-state logic element using micromagnetic simulations is performed. A general introduction to the simulation setup and the discussion of figures-of-merit is given. First, the dimensions of a rectangular element that suppress the formation of the undesired vortex state are discussed; then we optimize the dimensions of the added appendages; and lastly the influence of imperfections on the device characteristics are discussed. In the end, a range of optimal geometrical parameters is presented.

3.1 S-State Reconfigurable Logic Element

Ferromagnetic nanostructures are attractive components of room-temperature magnetic memory devices, logic devices [34, 35, 36, 6, 37], memory device and logic device combinations [38, 39], as well as their combinations with CMOS [40]. In the 1950s and 60s [41], magnetic logic devices were developed and they're experiencing a comeback mainly due to their non-volatility and comparably low-power consumption [42] in combination with the ability to perform logic, storage, and amplification in a single device [5].

The magnetic logic devices require stable magnetization state that can be switched in a binary fashion. The switching event can be inverting the rotation of a vortex state or switching the direction of a magnetization into the opposite direction. A large number of geometrical structures and materials are feasible, of which many have been explored both numerically and experimentally, like disks, symmetric and asymmetric rings, ellipses, triangles, trangle rings, Reuleaux triangles, and hexagons [43]. The concept of several sub-elements magnetistatic coupling into logic gate [44, 7, 6] is very promising. However, only a small number of these geological structures are turned out to be able to yield the desired operation [45]. Structures with shapes different from rectangular and ellipse lead to a more robust operation that is more tolerant to lithographic errors.

In Pampuch's paper [46], the dominant magnetization direction in manganese arsenide thin film can be switched as a function of two perpendicular magnetic input fields. A generalized concept of making use of common soft magnetic material Permalloy were presented in [47]. An S-state is a common magnetization state that can be found in Permalloy prisms in which magnetic moments assemble an "S" liked state. Structures and materials were discussed in our previous work [47] to support stable and useful S-state domain structures, and the S shaped Permalloy element with perpendicular magnetic fields were demonstrated the reconfigurable logic operation. It will also be shown in the following section.

S-state elements are potential magnetic random access memory (MRAM) [48]. Magnetoresistive memory is based on a magnetic film being in one of two possible magnetization states that can be switched by either applying perpendicular external magnetic fields [49] or spin torque transfer (STT) [50]. The read-out can be achieved in the magnetoresistive stack employing the GMR (giant magnetoresistance) [51] or TMR (tunnel magnetoresistance) effect [52]. MRAM has advantages like nonvolatility, endurance, and hight speed [53], but it also faces serious scaling challenges. The nanoscale magnetic elements have to be thermally robust, yet the switching fields has to be within practical limits. Other challenges are related to variations from element-to-element [54] and cycle to cycle [55]. S-state element could be a good candidate due to its robust and shape-stabilized magnetization state.

In rectangular and elliptical nanostructures, S state magnetization pattern and C state magnetization pattern are well known metastable states. The elongated nanostructures contain quasi single domain states that has abrupt switching behaviour and gives squarelike hysteresis loop. The C state can be generated by simply driving out a vortex state in the elongated structures, while the S state can be left by reducing the perpendicular field after the element reaching saturation magnetization.

The S-shaped magnetic logic element is presented in the work by Professor Hesjedal [47]. To utilize the interesting S state in a device, the control over the device is needed. Figure 3.1 shows the basic geometry of S-state element, two appendages are attached to the rectangular center body.

The remanent state of the S-state element of suitable dimensions, specially dimensions that suppress the formation of a vortex state, are shown in Fig. 3.2(a). The color scale corresponds to the value of the x-component of the magnetization (blue $\rightarrow M_x/M_s = 0$; red $\rightarrow M_x/M_s = +1$). The ideal (square-like), easy-axis hysteresis loops M_x^*/M_s^*, are shown in Fig. 3.2(b). The dashed line in this figure represents the unbiased curve. The curve shifts to the left for a negative applied external magnetic field in the y-direction.

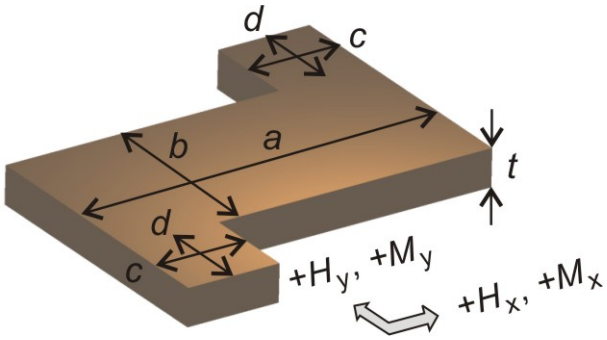

Figure 3.1: Illustration of the geometrical parameters of the S-shaped element. Center rectangle has dimensions of $a \times b$, and two appendages have dimensions of $c \times d$. The thickness of this element is 10 nm. The coordinate system is shown below.

For a positive applied external magnetic field in the y-direction, the curve shifts to the right. It is symmetric about the origin with the same amplitude of the y-direction external magnetic field applied. The vertical blue lines indicate the ideal perpendicular input fields, $\pm H_{s,x}$, that lie right between the respective biased and unbiased curve. Upon biasing the element by an appropriate field in $-y$-direction, $-H_{s,y}$, the curve gets shifted to the left, i.e., towards lower field values H_x (red). For a positive biasing field, $+H_{s,y}$, the curve gets shifted to the right, i.e., towards higher field values H_x (green). In other words, the magnetization reversal of the S-state element can either be delayed or advanced by a field perpendicular to the easy axis. In L-shaped structures, a similar hysteresis loop shifting behaviour has been reported [56].

At the right bottom corner of Fig. 3.2(b), the asterisk denotes the effective remanent magnetization of the center part of the structure. The central part, M^*, where provides the effective remanent magnetization is shown in the sketch in the lower right-hand side. This situation corresponds to attaching a spin valve structure on top of the central element for read-out. For the macroscopic magnetometry measurement, the resulting hysteresis curve would be around as a result of the magnetization in appendages that deviates from the

easy axis x-direction.

To obtain logic functionality, the two perpendicular input fields are treated as the independent inputs $A(H_x)$ and $B(H_y)$. Logic 1 represents in the x-direction to $+H_{s,x}$ and in the y-direction to $-H_{s,y}$; Logic 0 corresponds in the x-direction to $-H_{s,x}$ and in the y-direction to $+H_{s,y}$. For the output, the magnetization of the center part of the element is assigned to logic 1 and 0 for $+M_x$ and $-M_x$, respectively. In the Fig. 3.2(b), the vertical blue line indicates the optimal input fields in the x-direction.

In Fig. 3.2(c), it shows the truth table of S-state element. Assuming an output state $O = 0$ $(-M_x)$. When we now apply only positive fields, $+H_{s,x}$ and $+H_{s,y}$, i.e., input logic values $A = 1$, $B = 0$, the magnetization of the center part remains in its initial state and cannot be switched to $O = 1$. If A is changed to 0 which negative field $-H_{s,x}$ is applied and B stays the same 1, the output state remains the same and cannot be switched to $O = 1$. This means that the output does not change, irrespective of the perpendicular input $B = 0$ OR 1. If negative fields are applied, $-H_{s,x}$ and $-H_{s,y}$, i.e., $A = 0$, $B = 1$, the magnetization also remains in its initial state, $O = 1$. Now when both inputs are set to logic 1 which $-H_{s,x}$ and $+H(s, y)$ are applied, the output O is flipped to 1, i.e., $+M_x$. This tells us that under the condition of initial output state $O = 0$ S-state element is an AND gate.

If the initial magnetization of the central part of the element was 1, i.e., $+M_x$. The output state switches to $O = 1$ only when negative logic inputs $A = 0$ and $B = 0$ are applied, i.e., $-H_{s,x}$ and $-H_{s,y}$. For the other 3 input combinations, the output state remains the same $O = 1$. This is the characteristics of an OR gate.

The S-shaped magnetic element provides a complete truth table. It can carry out logic operations.

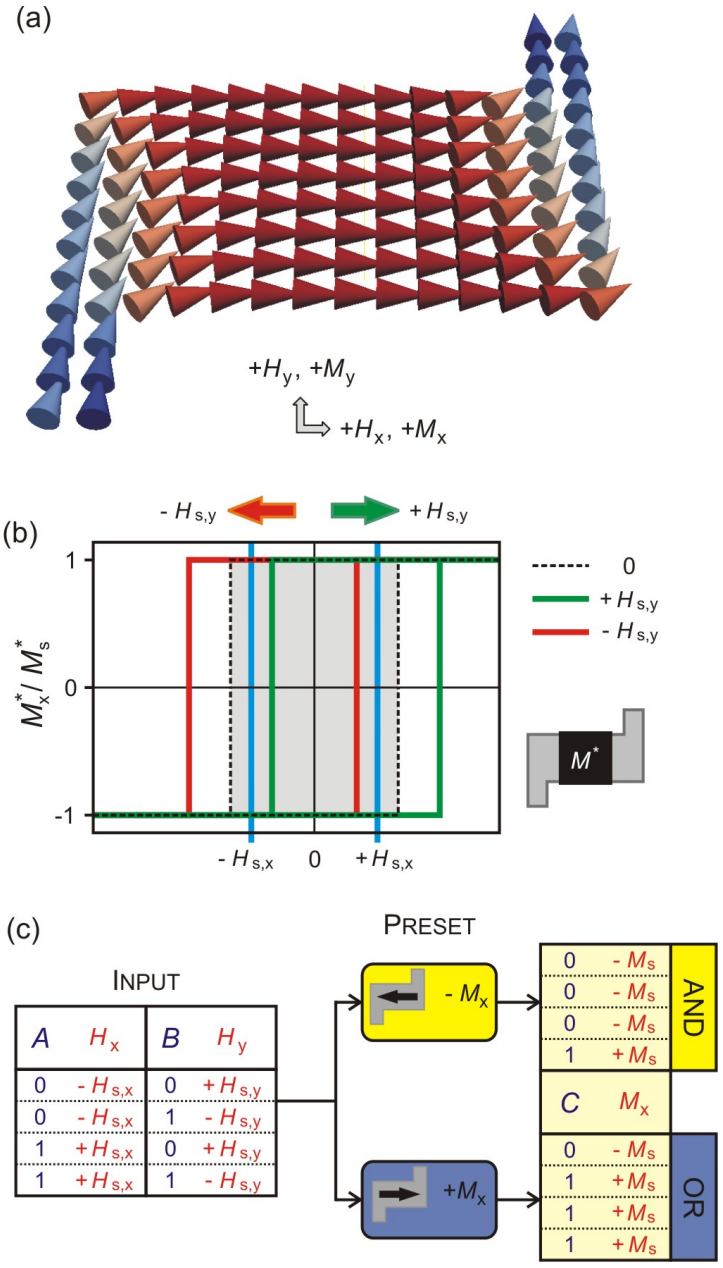

Figure 3.2: (a) Remanent magnetization distribution in a Permalloy S-shaped element. (b) Idealized hysteresis curve of a biased S-shaped element. (c) Logic table for the S-shaped element.

3.2 Simulation Setup

The geometric parameters of S-shaped element play an important role in stabilizing the logic functionality. The goal of the work in this section is to establish geometrical stability criteria for S-shaped logic elements. We start with the simplest, symmetric structures which will lay the foundation for more complex, independent input variations in the future. The basic structure consists of a rectangular center part with dimension $a \times b$ and two appendages symmetrically attached to the center body with dimension $c \times d$, as shown in Fig. 3.1. Two appendages will be able to vary in shape and area, and respond to input field in the y-direction will be different. Asymmetric appendages add additional degree of design freedom.

The micromagnetic simulations were performed using Scheinfein's LLG simulator [57]. For the investigation of the Permalloy structures, the following micromagnetic constants were used: a saturation magnetization of $M_s = 800$ emu/cm^3, an exchange constant of $A = 1.05 \times 10^{-6}$ erg/cm^3, and a uniaxial anisotropy constant of $K = 1000$ erg/cm^3. The simulations were carried out on a Cartesian grid with $\Delta x = \Delta y = \Delta z = 5$ nm at 0 K.

To utilize the the S-state element, it has to be integrated into a suitable device structure. The most simple realization comprises address lines providing perpendicular Oersted fields for the inputs, and a magnetoresistive readout structure. Hereby the S-state element will be the free layer in a magnetoresistive trilayer structure, such as a giant-magnetoresistance (GMR) [51] or spin-dependent tunnelling (TMR=tunnel magnetoresistance) [52] device. To optimize the read-out signal, the magnetization in the section of the S-state element that is part of the magnetoresistive element should be fully in the x-axis direcrion. For exploring the usable geometrical parameter space, the following general criteria have to be taken into consideration:

- In magnetoresistive trilayer structures, the projection of the free layer can be effec-

tively read out. For optimizing the read-out signal, the projected magnetization of the central part of the S-state element has to be fully aligned with the fixed layers in the magnetoresistive stack. Thus, the hysteresis loops should be square-like, i.e., M_r/M_s should be close to unity and the roundedness of the shoulders should be small. This limits the relative size of the appendages over the center rectangle which should not be too large which causes value reduction of M_r/M_s.

- The first criterion implies that the magnetization state in the center rectangle is quasi single-domain. This requires the rectangle to be below a certain size, and to have a rather elongated shape, in order to avoid the formation of a vortex state.

- The functionality of the S-shaped element depends on a sufficiently large shift of the hysteresis due to the biasing field $\pm H_y$. The sufficient large shift results in a more reliable operation and less stringent fabrication requirements, so that small shifts of the coercive field due to structural imperfections, such as rounded edges and sidewall roughness, can be tolerated.

- Ideally, the coercive fields applied to the x- and y-directions should be of the same magnitude, or, to be more precise, the driving fields used to switch the elements should be as symmetric as possible. This adds another criterion to the relative size of the appendages over the center rectangle.

- The coercive field has to be chosen in a proper range. If H_c is too large, the switching process will require too much energy so this device is expensive from perspective of the energy cost. If H_c is too small, the element will be unstable due to relatively large magnetic field noise or relatively large imperfection caused by fabrication imperfection.

3.3 Remanent Magnetization Patterns in Rectangular Prisms

To systematically study parameter space of the S-state element, first, we investigate the parameters of the center rectangle. As we mentioned before we have the center rectangle with dimension $a \times b$. To integrate the S-state into a standard magnetoresistive layer structure requires the magnetization in the center rectangle that overlap with the magnetic sensor stack to be quasi single-domain. Besides, to prevent the demagnetization due to thermal fluctuations, single-domain state in the center rectangle is also desirable.

The remanent state of rectangular Permalloy prisms have dependence of the thickness and size [58]. In specific geometry, quasi-homogeneous sigle-domain states and demagnetized flux-closure patterns can exist in the length range between 250 and 1000 nm. In Permalloy rectangles, common quasi single domain patterns are S-state and the C-state. Common flux-closure patterns are the Landau state (one vortex) and the diamond state (two vortices). Stray field energy which favours flux-closure patterns and exchange energy which favours homogeneous magnetization compete with each other. The competition between stray field energy and the exchange energy determines if flux-closure patterns exhibit. In general, as structure size becomes smaller, the exchange energy becomes more significant than the stray field energy, and the stray field-reducing flux-closure patterns are less common due to their relatively high exchange energy.

In the most general cases, lateral dimensions, thickness, and magnetic material properties determine the details of the phase diagram of remanent magnetization patterns. In our analysis, thin Permalloy films which are commonly used in practical device applications were used. The magnetization pattern in soft magnetic Permalloy is largely dependant on the shape anisotropy which determines the stray field energy distribution [23]. Theoretically, the thickness of thin film doesn't affect the energy density of a thin film element

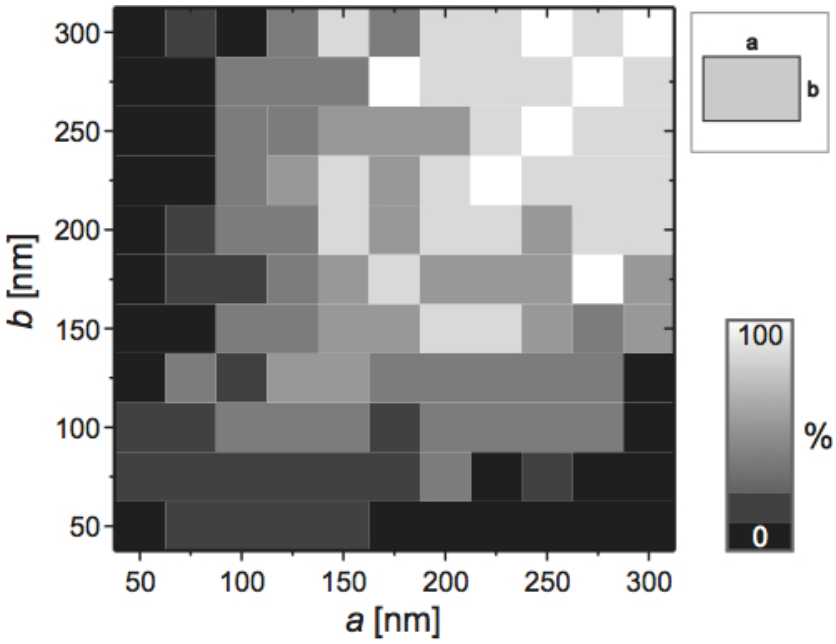

Figure 3.3: Investigation of the remanent magnetization of rectangular thin-film elements of dimensions $a \times b$. The grey value gives the probability of vortex or other flux-closure domain formation obtained from 10 simulations starting from different random initial magnetizations.

supporting a multi-domain flux-closure patterns,but it still favours S- and C-state patterns due to overall relative importance of the stray field energy [58]. We chose a film thickness of 10 nm, which is an upper bound for typical ferromagnetic layers in magnetic tunnel junctions [59].

The sampled parameter space stretched from minimum lateral dimensions of 50 nm and reached up to 300 nm (side length). According to the phase diagram for 10-nm-thick rectangular prisms [58], a C-state should provide the lowest-energy configuration for the chosen lateral dimensions from given parameter space. Here we want to test the stability of the element and the suppression of flux-closure patterns. For any given shape, we relaxed the magnetization starting from completely random configuration for any given shape and

repeated for ten times. The times that forms a flux-closure pattern were counted and the results of the simulations were plotted as a function of length, a, and width, b, in Fig. 3.3. The grey values indicate the likelihood of finding a flux-closure pattern in the rectangle prisms. From the Fig. 3.3, we can tell that the probability of vortex formation increases as the area increases, and is higher for more square-like structures ($a \approx b$). Away from the square-like structures, we can tell that elongated structures suppress the vortex formation. As the lateral dimension extends, the grey value increases so there will be a upper limit for the lengths. At a thickness of 10 nm, useful rectangular prisms should have a maximum dimension of the smaller length of ~ 125 nm.

In order to stabilize the S-state or C-state, and to increase the usable parameter range, we can biasing the center rectangular prism with adjacent magnetic elements to force the formation of S-state or C-state, e.g., used in magnetic logic arrays [6]. The adjacent elements make magnetostatic dipole coupling with center rectangle. Instead of adding adjacent elements, add magnetic material at selected locations. This method can stabilize the preferred states as well and avoid the fabrication challenges associated with narrow gaps. Here we chose S-state pattern over C-state pattern. Generally the S-state pattern has an advantage over C-state pattern. For S-state pattern, the magnetization direction of the added elements (appendages) is pointing in the same direction, which allows to apply an external field globally instead of locally to each appendage. But if local magnetization reversal techniques such as spin torque transfer are employed, the C-state element gives a larger versatility.

Figure 3.1 shows the general layout of S-state element. The appendage size should neither be too small as a sufficient biasing effect need to be achieved, nor too large as this would lead to a reduced project along the x-direction or deform the magnetization pattern in the center of the structure. A reasonable compromise is using 40×50 nm^2. The S-state elements with variable center rectangle size and fixed appendage size, 40×50 nm^2.

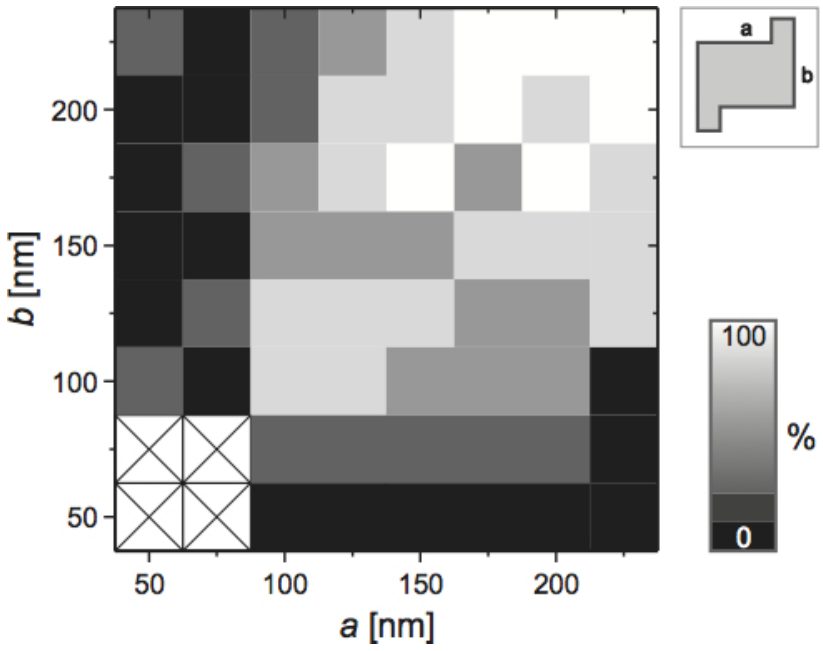

Figure 3.4: Investigation of remanent magnetization of rectangular thin-film elements of dimensions $a \times b$ with fix appendage size ($c \times d = 40$ nm$\times 50$ nm). The grey values represent the probability of vortex or flux-closure domain formation obtained from 10 simulations starting from different random initializations.

To test the stability of S-shaped element and the suppression of flux-closure patterns, we relaxed the magnetization starting from the completely random configuration and repeated the simulation ten times. The result of simulation is plotted as a function of center rectangle prism lateral dimensions a, the length, and b, the width, as shown in Fig. 3.4. Also, the grey values indicate the likelihood of forming a flux-closure pattern. Compared with the case without appendages (Fig. 3.3), the structure becomes more unstable from the perspective of flux-closure domain formation. Also, even the smaller square-like structures will more likely develop vortex patterns. This is an important detail that we need to bear in mind, as it is counterintuitive that the presence of appendages increases the probability of forming vortex states. Nevertheless, the addition of the appendages is essential for optimizing the effectiveness of the perpendicular in-plane field.

After analysing Figure 3.3 and Figure 3.4, additional restrictions on the center rectangular prism parameter space are added. Naturally, as the structure gets longer, a lesser tendency towards vortex formation is observed. In this section, we used completely random magnetization as initial input, while, during operation of the device, the element is never coming out of a completely random magnetization state. As a result, the element will be much more stable against spontaneous vortex formation. If, for example, a useful minimum feature size of 100 nm is assumed for the rectangle, the longer side should be at least 150 nm long. The aspect ratio of the rectangle should thus at least 1.5:1.

3.4 Influence of the Rectangular Aspect Ratio a:b

The size and aspect ratio of the center rectangular prism have to be chosen so that both coercive field and the remanent magnetization are in useful ranges.

For this investigation, the appendage size was again set to 40 nm$\times$50 nm and the aspect ratio of the rectangle as a parameter was varied. Fig. 3.5 shows the plots of the reduced

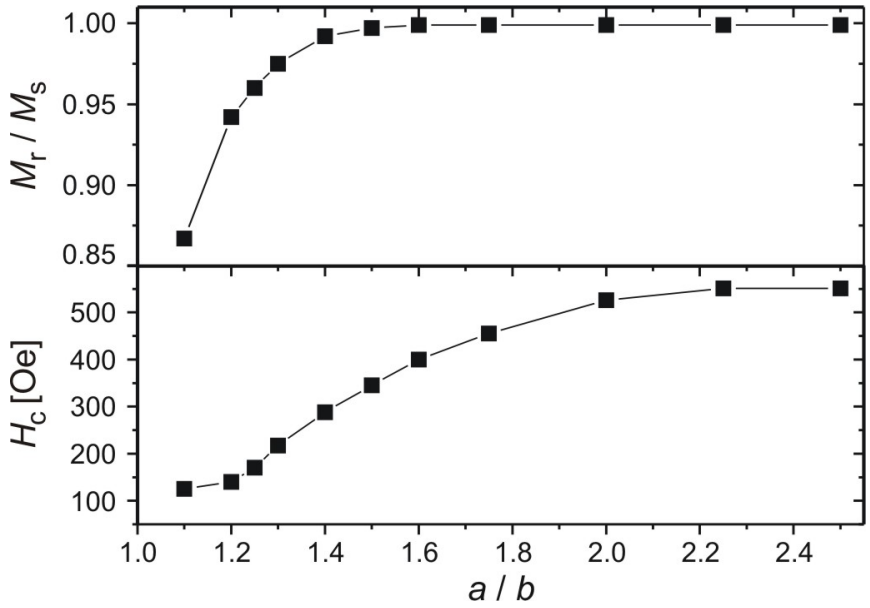

Figure 3.5: Plot of coercive field, H_c, and reduced remanent magnetization, M_r/M_s, of S-state elements as a function of length of the center rectangle, a. The rectangle width is fixed at $b = 100$ nm and the appendages are measuring 40 nm$\times$50 nm.

remanent magnetization, M_r/M_s, and the coercive field, H_c, as a function of a/b for a fixed width of $b = 100$ nm, obtained from the hysteresis loops. In this plot, the reduced remanent magnetization is measured an area of 100×100 nm^2 in the center of the rectangle, which is the assumed size of the magnetoresistive sensor element, shown as area of M^* in Fig. 3.2(b).

As a high reduced remanent magnetization of close to unity is desirable for large read-out signals of the magnetoresistive sensor, an aspect ratio of at least 1.4 has to be chosen. Above the requirement of high reduced remanent, however, the coercive field is already approaching 300 Oe, while the smaller fields of ∼150 Oe as shown in the plots would certainly be better in terms of power requirements.

3.5 Study of the Appendage Size

In this section we optimized the appendages in terms of overall area and aspect ratio. To investigate the influence of ear size, we kept the center rectangle fixed at $a \times b = 150 \times 100$ nm^2. Figure 3.6 shows the plot of remanent magnetization (a) and the coercive field (b) of S-state elements as a function of the aspect ratio c/d of the appendages and for five different appendage areas ranging from $c \times d = 1000$ to 3000 nm^2.

When the aspect ration c/d increases for the given appendage area $c \times d$, M_r/M_s and H_c generally decrease. For a fixed aspect ratio, M_r/M_s and H_c also decrease as the area increases. When the appendage aspect ratio c/d is between 0.2 to 1.25, the coercive field values remain rather similar at a value between 300 and 500 Oe. The reduced remanent magnetization stays above 90%, except for large appendages (2500 and 3000 nm^2) If the aspect ratio is further increased beyond 1.25, the coercive field decreases dramatically, which means that there is not enough effective biasing due to the appendages. The reduced remanent magnetization follows the same trend, however, the slope is not as steep for

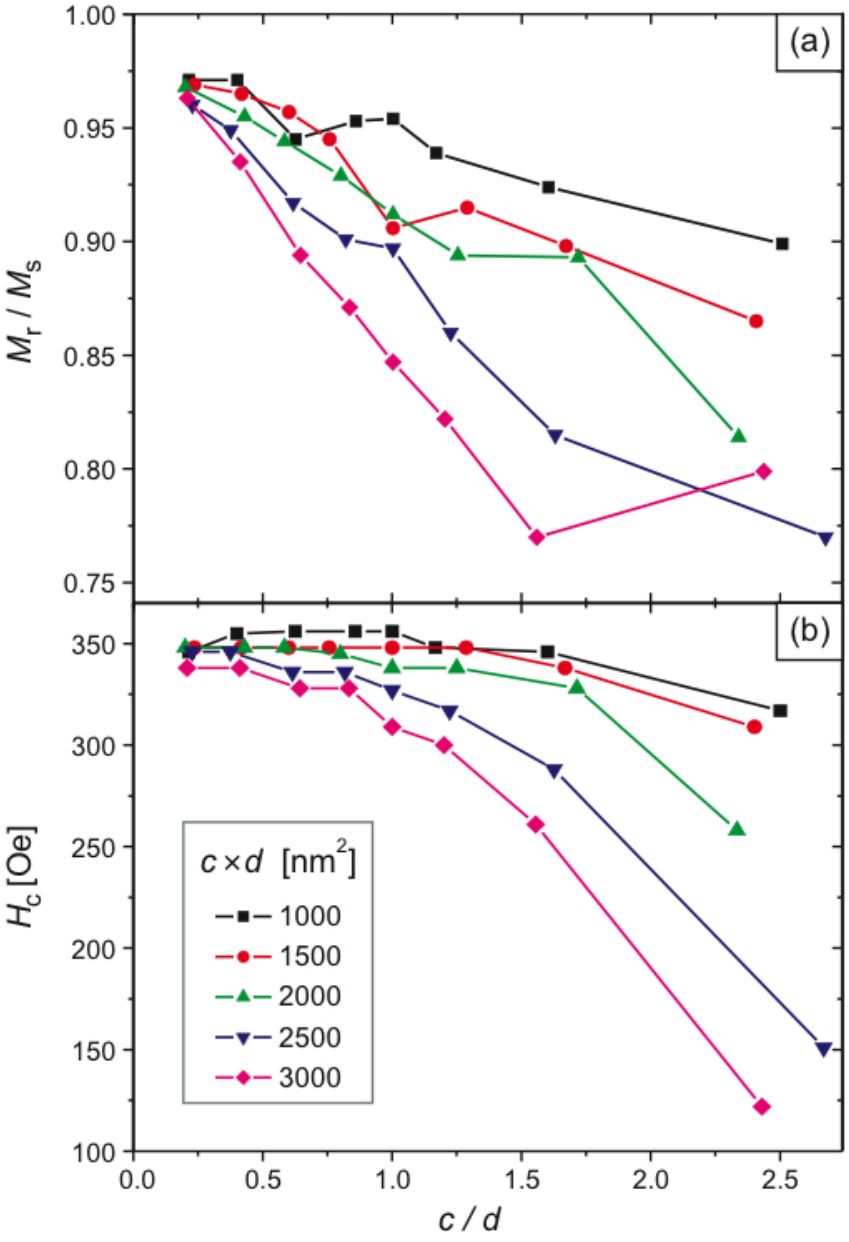

Figure 3.6: Plot of coercive field, H_c, and remanent magnetization, M_r/M_s, of an $a \times b =$ 150 nm×100 nm S-state element with varying appendage size on the form factor c/d, of the appendages. Plots are shown for five different appendage areas $c \times d$.

smaller appendages. decreases with a less steep slope than coercive field.

In summary, appendages with areas of 1000 to 2000 nm^2 stabilize the S-state in the center of the structure well for aspect ratios of up to $c/d = 5/3$, while the reduced remanent magnetization stays above 90%.

3.6 Study of Imperfections

The imperfection of the S-state structure created during fabrication will give rise to undesired shifts of the hysteresis curves [60]. Within soft magnetic thin films that have vanishing magnetocrystalline anisotropy, their magnetic properties are dominant by the shape anisotropy. Therefore, the size and shape variations introduced by fabrication-related imperfection will be the most important to consider. In this section, the side wall roughness and edge roundness were investigated in detail. Other imperfections that are not considered here, are deposition-induced surface roughness, etching-induced tilted surface edges [61], diluted magnetization near the edge due to oxidation [62], surface anisotropy [63], and deposition-induced material anisotropy.

In order to find how imperfections affect the reliability of the S-state element, we investigated two idealized types of imperfections, roundedness of the edges and the roughness of the sidewalls. As shown in Fig. 3.7(a,b), the S-shaped structures consist of 150×100 nm^2 rectangles with two 40×50 nm^2 appendages. In (a), all the corners in this structure are rounded as it commonly occurs in overexposed structures obtained by electron beam lithography. A rounding radius of $R = 20$ nm was assumed. In (b), a regular roughness pattern was added to the sidewalls of the element. The defects have lateral dimensions of 5×5 nm^2 on the edge and are separated by distance of 10 nm. In both cases, the volume of the magnetic material remains the same as the unaltered structure.

Hysteresis loops were obtained for structure (a), (b) and ideal S-shaped element. For

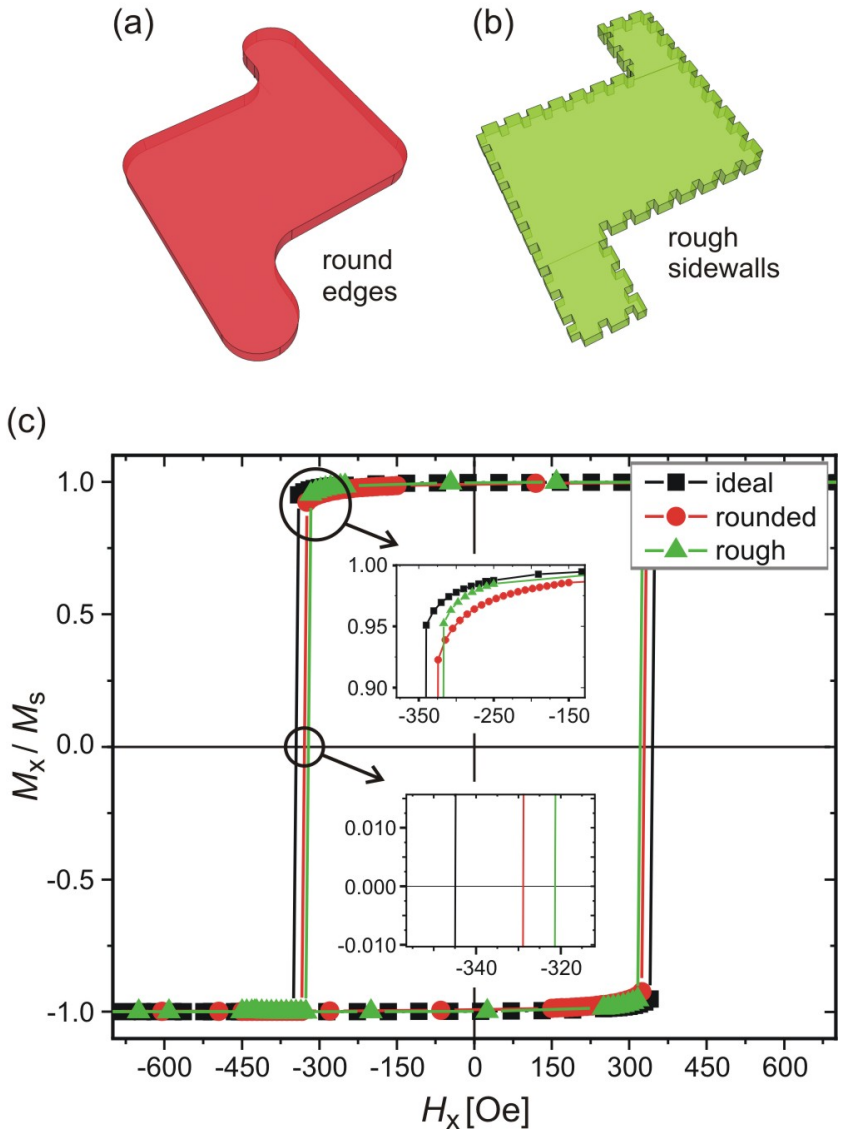

Figure 3.7: (a) and (b) illustrate S-shaped elements with sidewall roundness and roughness separately. (c) shows the influence of imperfections on the hysteresis loop of an $a \times b =$ 150 nm×100 nm S-state element with $c \times d =$ 40 nm×50 nm appendages. Hysteresis loops of ideal and imperfect S-state elements is plotted. The characteristics remain similar with slightly deviations of the coercive fields of below 7%.

a ideal S-state element with perfect geometry structure, the coercive field is 348 Oe. The coercive value reduces to 329 Oe for the element with rounded corners and to 302 Oe for element with rough sidewalls. In (c), close-ups show the effect of the imperfections on the roundedness of the hysteresis loop in greater detail. None of the considered imperfections alters the hysteresis curve for the selected element qualitatively. The two types of imperfection give hysteresis loop shift up to 46 Oe. Bear the shift value 46 Oe in mind, to guarantee the switching events during logic operation correctly occur, the hysteresis loop shift created by biasing field has to be significantly larger than 46 Oe. We note that the shift of the coercive field is sensitive to sidewall roughness especially when the vortex motion is part of the reversal process.

Simulations of perfect and imperfect rectangles with length of 150 nm and width 100 nm were carried out. For the rectangle with perfect structure, coercive field of 343 Oe was obtained. The reversal proceeded via C-state formation which lead to the roundedness of its hysteresis curve, and switched abruptly at coercive field via the creation, propagation, and annihilation of a vortex state. The reversal process with formation of S-state is quite similar to the reversal process with formation of C-state, except that it has slightly higher coercive field 347 Oe. In contrast to this behaviour, rough rectangle tended to pin the initial C-state. The hysteresis loop shows that, after the initial roundness, a linear decrease that persists even down to negative values of the magnetization, before the abrupt reversal happens at a values of 443 Oe. Within reasonable limit, it is found that the detail of edge roughness, i.e., magnitude and frequency of the defects, do not affect the principal reversal process; and the coercive field values typically range from 347 Oe and 590 Oe. We can see that the range of coercive field of simple rectangle is at least twice as large as in the case of S-state element.

To obtain the trend of coercive field shift as a function of geometry and defects, a set of simulations was carried out on selected S-state configurations. The results are summarized

	a [nm]	b [nm]	c [nm]	d [nm]	ideal [Oe]	round [Oe]	rough [Oe]
S	150	100	40	50	339	345	335
S	150	100	45	45	348	354	343
S	150	100	60	35	299	301	303
S	190	125	40	50	323	325	303
S	190	125	45	45	325	327	309
S	190	125	60	35	329	329	301
R	150	100	-	-	343	347	443
R	190	125	-	-	313	319	295

Table 3.1: Influence of roughness and edge roundedness on the coercive field of S-state structures (S) and regular rectangles (R).

in Tab. 3.6. The values in given table are the average coercive field obtained from five simulations. The center rectangle has dimensions of a and b and the appendages are defined with dimensions c and d. The results for the ideal structures, the rounded structures (radius 20 nm), and the rough structures are shown in this table. Please note that a different roughness algorithm is applied here with the roughness algorithm in Fig. 3.7.

In general, rounded edges do not affect hysteresis loop as much as rough edges. The effect of roughness further depends on the detail of reversal process. Further, comparing the two rectangles, the larger one is less prone to roughness effect than the smaller one. For larger rectangle, the S-state can accommodate and can be switched by rotating over the edges. For smaller rectangle, C-state that is created during reversal process can get easily trapped by defects. Another obvious trend is that structures that do not have long protruding appendages are less prone to equally sized defects than the structures with long protruding appendages.

3.7 Optimization of the Biasing Field

In this section, we will discuss the choice of the biasing field and the influence of the geometrical parameters on its optimum value. The biasing field H_y is one of the inputs required for the logic operation. It is perpendicular to the easy axis of the rectangular center prism. As it is known from last section, geometric imperfections will lead to an undesired shift of the hysteresis loops that compromises the function of the device. So, the coercive field shift, the effect of the biasing field, has to be sufficiently larger than all distortions combined.

To study the biasing field effect, different structural configuration were analysed. The rectangular center structure has a fixed width of $b = 100$ nm and a variable length a leading to aspect ratios of $a/b = 1.25$, 1.50, 1.75, and 2.00. For the two appendages, size 2000 nm^2 was chosen with different form factors of $c/d = 0.2$ (20×100 nm^2) to 2.33 (70×30 nm^2) were selected. The choice of parameters was governed by the results obtained and discussed in the previous subsections.

Because of the biasing, every hysteresis loop has now two distinctly different coercive field values. For simplicity, H_c always refers to the larger of the two values of the coercive fields. The overall shift of the hysteresis loops is expressed by $\Delta H_c = |H_c(+H_y) - H_c(-H_y)|$. From the previous section, we obtained a coarse estimate of the imperfection-induced coercive field shift of 48 Oe. As this shift occurs in both biasing directions, ΔH_c has to be at least larger than 96 Oe which doubles 48 Oe. For convenience, 100 Oe contour line is outlined in Fig. 3.8.

Figure 3.8 shows contour plots of the coercive field shift ΔH_c as a function of rectangular aspect ratio, a/b, and appendage aspect ratio, c/d, for three different values of the perpendicular biasing field H_y. The three plots correspond to a H_y of 50 Oe (a), 100 Oe (b), and 150 Oe (c). In all three plots, the 100-Oe-limit contour defines acceptable geom-

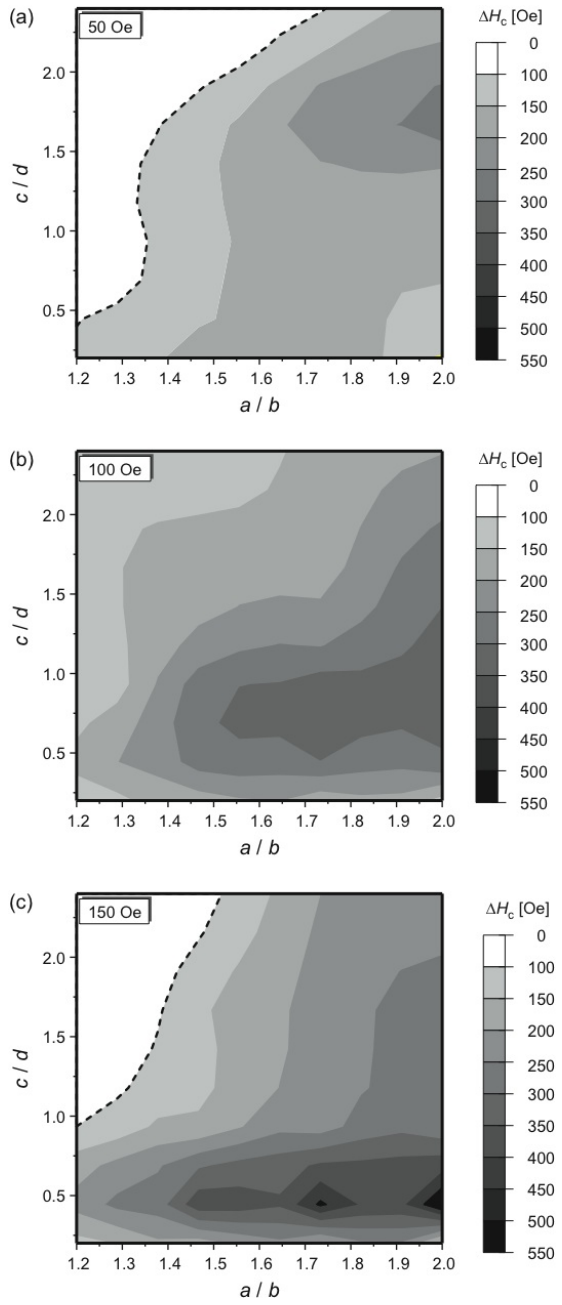

Figure 3.8: Shift of the coercive field, ΔH_c, as a function of rectangle form factor, a/b, and appendage form factor, c/d. The results for three different biasing fields, H_y, are shown: (a) 50 Oe (b) 100 Oe, and (c) 150 Oe. All elements have the same body width $b = 100$ nm and appendage area $c \times d \approx 2000$ nm^2. Dash lines indicate the 100-Oe-limit.

etry areas. The unusable areas are where the shift is less than 100 Oe. In general, the coercive field shift ΔH_c increases with the value of a/b, while its c/d dependence shows more pronounced maxima and minima. For $H_y = 50$ Oe (a), acceptable aspect ratios are linearly increasing with the a/b ratio. For $a/b = 1.2$, the c/d has to be chosen under 0.4 while for $a/b > 1.75$ the entire tested c/d range is usable. For $H_y = 100$ Oe, H_c is by choice always larger than H_y. H_c differences remains small. For $H_y = 150$, acceptable aspect ratios are confined to an area below a line reaching from $c/d = 0.8$ at $a/b = 1.2$ to $c/d = 2.5$ at $a/b = 1.5$. Remarkably, large shifts ΔH_c are found for $c/d \in [0.4, 0.6]$ and $a/b > 1.45$.

Another design criterion for S-shaped logic element is that biasing field and coercive field should have roughly the same magnitude. If the rectangular aspect ratio is chosen to be greater than 1.4, the coercive field H_c (without biasing field) is roughly between 300 and 550 Oe (cf. Subsec. 3.5). After adding the biasing field H_y, the (larger) coercive field value $|H_c + \Delta H_c|$ will be in the interval $[300 + \Delta H_c, 550 + \Delta H_c]$. If, for instance, $\Delta > 450$ Oe the coercive field can become greater than 1000 Oe, which by itself is a large value and also much larger than the other input field value. Since ΔH_c generally increases with a/b, the upper limit of acceptable ΔH_c values will also give an upper boundary for the aspect ratio a/b.

For the appendages, the areas in which the coercive field shift ΔH_c is larger than 100 Oe is somewhat more complex. When the aspect ratio c/d of the appendages is too large, they will effectively become a part of the rectangular prism and simply increase its width b by $(2 \cdot c)$ - without having a biasing effect on the central structure. If $c : d$ is too small, the appendages become too small to sufficiently alter the magnetization pattern of the center structure. The upper and lower bounds for $c : d$ are clearly visible in Figure 3.8(b,c), whereas the upper cut-off in (a) is beyond the simulated parameter range. Also note that the contact area between appendages and rectangular prism, c, is limited by the choice of

discretization length, which is 5 nm for the present simulations. A length of 5 nm agrees well with exchange length in Permalloy of 5.3 nm.

3.8 Discussion

The commonly known S-state magnetization pattern in soft magnetic thin film elements is an interesting feature. It can be exploited for magnetic logic operations. The working principle of S-shaped element is the shift of the hysteresis loop of the rectangle due to the applied perpendicular in-plane fields which is along the width of the center rectangle. Two inputs are provided to address the element and obtain logic operation.

In rectangular Permalloy prisms with a thickness of $t = 10$ nm, the S-state pattern is not a minimum energy configuration. Two appendages were added to the center rectangle to force the element into an S-state magnetization pattern as the lowest energy configuration. So, as a first step, the rectangular prisms were chosen as to suppress the formation of vortex and other closed-flux domain patterns. In general, it requires that the structure should be (i) small, as the exchange energy becomes relatively more important in small structures and disfavours domain formation, and (ii) elongated, as elongated rectangle prism leads to the formation of a disfavoured magnetization direction thereby suppressing some, but not all, flux-closure patterns. While stretching the rectangle increases value of coercive field, which eventually affects the integration density due to the large required switching fields. Although small center rectangle favours the desired S-state magnetization, the inner area that is to become free layer in a magnetoresistive layer stack needs to match with the commonly used, or anticipated, GMR or TMR sensor footprint. As a minimum feature size of 100 nm has been common in TMR elements for some time now [64]. The same size has been chosen for the width of the center rectangle in this investigation. As part of this device integration it has been made sure that the magnetization in this area is fully aligned

with the long axis of the rectangle to maximize the read-out signal.

The appearance of the appendages certainly affects the magnetization pattern of the rectangular prism. Obviously, very small, as well as very large, appendages will not stabilize an S-state. In the case of very small appendage size, they would be simply too small to make difference. In the other case which the appendages are comparably large, they could be so big that they essentially become an integral part of an enlarged rectangle. A good compromise is an appendage area of 1000-2000 nm^2.

Two inputs are provided to address the element and obtain logic operation. The two inputs can use the straight-forward way in which current-carrying wires proving sufficiently large Oersted fields. As the fields have to be crossed, the two write lines would have to be placed for example above and below the S-state element. Another way to apply the two inputs is using spin torque transfer (STT) [50]. This includes not only the central rectangle, which needs to contacted by a GMR or TMR sensor, but also the appendages. This solution, although elegant, poses serious fabrication problems as three separate STT structures would be needed that would have to be very close together. Further, as non-collinearly magnetized reference layers are needed two separate fabrication process runs for the STT-driven GMR or TMR stacks are needed.

Another noteworthy feature of S-state element is its relative reproducibility of switching behaviour, and thus the coercive field values. Compared to S-state element, the simple rectangle gives larger deviations on coercive field values in simulation. The reason why added roundness and roughness defects do not affect S-state element to the same degree with simple rectangle might lie in the fact that appendages can be seen as defects which dominant the nature of the switching process. The edge defects have relatively less impact. In fact, the magnetization reversal of S-state structures always proceeds via rotations of the magnetization in the appendages, while magnetization reversal of simple rectangles would strongly depends on the detail of defect structures. Therefore, it is conceivable that

S-state element might be employed in MRAM cells as they have potential to reduce the element-to-element and cycle-to-cycle variations in the switching field.

3.9 Summary

In this chapter, I presented a detailed micromagnetic analysis of the useful geometrical parameter space for S-state magnetic logic elements. An S-state element essentially relies on the biasing effect of a perpendicular in-plane field on its hysteresis loop, which is a shift of the coercive field. We defined several design criteria that are critical for the logic operation. The size and aspect ratio of the center rectangular prism were chosen so that flux-closure magnetization patterns are suppressed. A good choice is a maximum width of the rectangle of 125 nm and a length that is at least $\approx$ 190 nm, using form factor of 1.5. In order to force the formation of an S-state pattern and maximize the effect of a perpendicular biasing field on the magnetization characteristic, appendages were attached to the rectangular prism. Each appendage should have an area between 1000 and 2000 nm^2, and an aspect ratio of up to 5/3. It is important to simultaneously attempt to maximize the alignment of the magnetization of the central part of the rectangle along the easy axis direction. The effect of biasing field was investigated together with a variation of the geometrical parameters. At the biasing field between 150 Oe and 200 Oe, while keeping the perpendicular field at the same range, the element with a large selection of geometrical parameters will perform the logical operation.

Chapter 4

Self-assembly of Magnetic Nanowires

4.1 Introduction

Magnetic nanowires are highly attractive materials that have potential for applications in ultrahigh magnetic recording, logic operation devices, and micromagnetics and spintronics sensors. In order to fabricate these potential devices, one of the challenges is to find a way to pattern these nanowires controllably and effectively. There are two basic approaches: top-down and bottom-up. For the pre-synthesized nanostructures, bottom-up assembly is the way to build nanodevices.

In this chapter, ferromagnetic nickel nanowires are synthesized by electrodeposition. Ni nanowires with a diameter of 200 nm are terminated by Au end caps in order to allow for further etching. Magnetic alignment is a facile technique for assembling nanowires into hierarchical structures [21]. It is an appealing approach which is capable of aligning thousands of nanowires in two dimensions. From the micromagnetic point of view, one major question that needs to be addressed is how the nanowires respond to external magnetic fields - either due to other nanowires in an ensemble or additionally added magnetic fields. Here, we investigate the magnetic remanence and reversal properties in

nickel nanowires by means of micromagnetic simulations. The technique of nickel nanowire synthesis is introduced. With synthesised nanowires, one-dimensional and two-dimensional alignments are successfully performed, and attempts have been make to align nanowires in three dimensions.

4.2 Simulation of Individual Nickel Nanowires

Micromagnetic simulations help us to gain insight into the magnetic behaviour of magnetic nanowires. The magnetic behaviour of nickel nanowires is diameter dependent [65]. In this chapter, 200-nm-diameter nickel nanowires are systhesised and all the micromagnetic simulations and experimental work are all performed at this particular diameter. I investigate its magnetic remanence and reversal properties by using the micromagnetic simulator Magpar. Because of the symmetry and simplicity of the fabricated nanowires, cylindrical geometries are particularly suited for the micromagnetic simulations of our nickel nanowires. The Magpar-simulator using FEM was used to carry simulation on well-meshed cylinder structures. The simulations presented in this chapter use the literature values for saturation magnetization, exchange constant and damping constant [7].

4.2.1 Relaxation and Reversal Dynamics of Single Nickel Nanowire

Studying the relaxation process of Ni nanowires is the starting point of understanding their alignment behaviour. In Magpar, a simple 200-nm-diameter cylinder with finite element meshes was used as input structure, and an random initial magnetization was given, shown in Figure 4.1 (a). The initial state of the simulation is given by all moments being randomly distributed. Note that the magnetic moments are all equal in strength. the magnetic moments in the cylinder start to relax from the random initial magnetization; (b) shows a transitional state and (c) shows the final state where vortices are formed along the

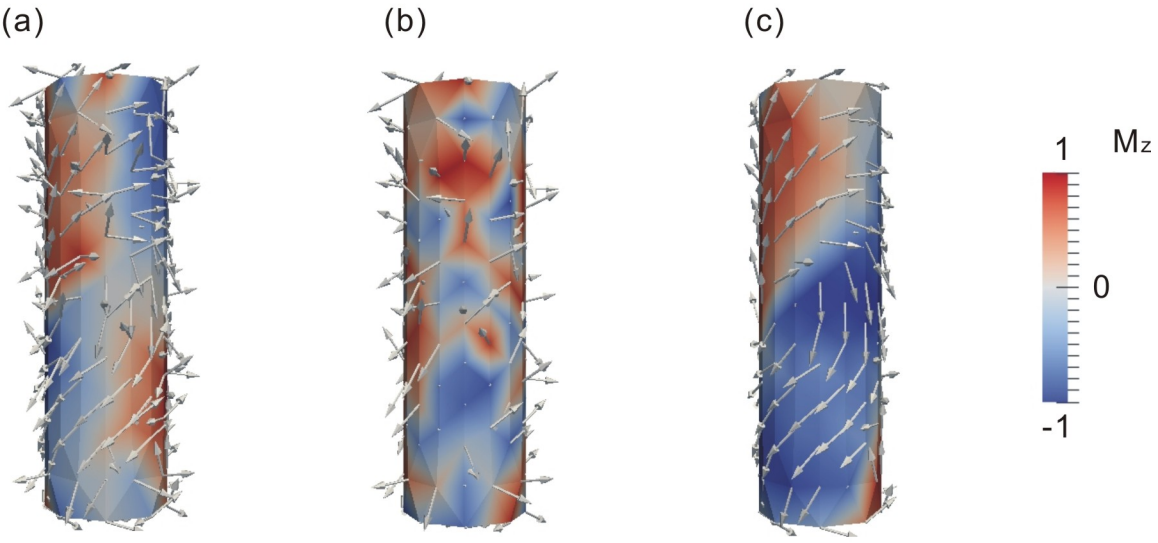

Figure 4.1: Snapshots of relaxation from random initial magnetization. The random initial magnetization shows in (a). In (c) the final state is shown and (b) is a snapshot between (a) and (c). The color legend at the right-hand side represents the projection of magnitization along z-axis.

ruled surface of cylinder. During the relaxation, magnetostatic energy and exchange energy battle against each other. Although a single domain would minimize the exchange contribution to the total energy, it will raise the total energy by increasing magnetostatic energy. Domain formation will lower magnetostatic energy while increasing exchange energy. From the simulation results, the formation of domain closures allows our 200-nm-diameter nickel nanowire to minimize its total energy.

Figure 4.2 are the snapshots of the relaxation process with saturated magnetization as initial state. (a) shows the nanowire at initial state with saturated magnetization along z-axis. (b-f) shows the transitional snapshots. We can see the vortices start forming at

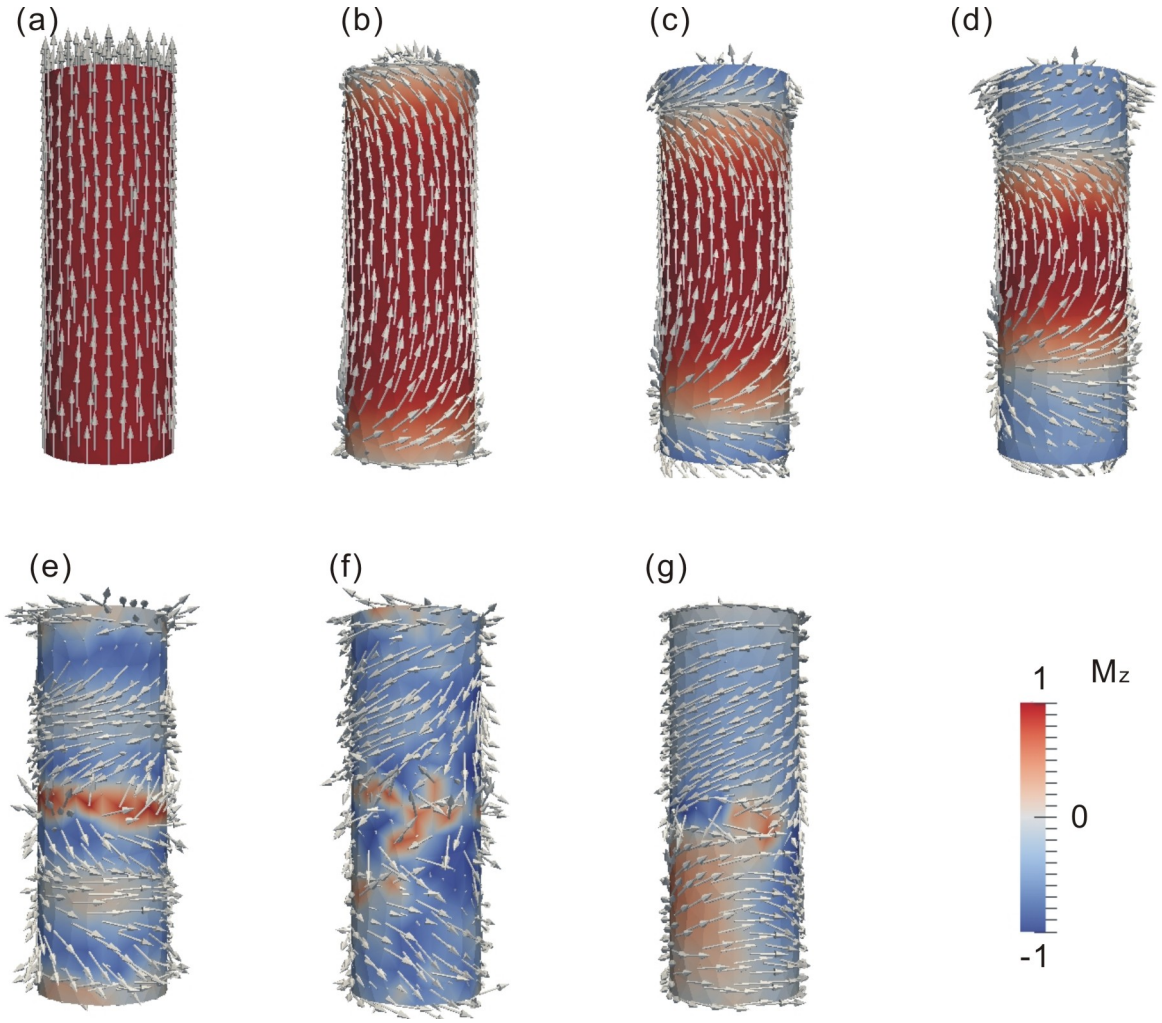

Figure 4.2: Remanent magnetization relaxed from saturated magnetization along z-axis. (a) to (g) are the snapshots from starting point to final state. The color legend on the right bottom corner represents the projection of magnetization along z-axis.

the two ends of the nanowire while the body center is still generally magnetized along the easy axis in (b-d). The color legend on the right bottom corner of Figure 4.2 and the right-hand side of Figure 4.1, represents the projection of magnetization along z-axis. The magnetization values are the normalized values over saturation magnetization M_s and between the range of [-1, 1].

To further study the magnetic properties of 200-nm-diameter nickel nanowires, the magnetic reversal is investigated here. During alignment, the nickel nanowires are magnetized by external field, and eventually after alignment, the external field has to be removed. Here we want to see how the nickel nanowires are magnetized and how the magnetization of those wires will change after removal of the external field.

A large external magnetic field pointing to $+z$-direction is applied to the nanowire, which the external field is along the cylinder axis. The applied external magnetic field is quite large at the beginning which magnetizes the nanowire to saturation state, $M_z = 1$ shown in Figure 4.3(a). Then we gradually reduce the external magnetic field, the reversal process starts by the nucleation of the two ends and subsequently propagates along the cylinder axis. As the field reduces to 0, the magnetization shown as (d) in which the magnetic moments forms vortices and the cores of these vortices parallel with cylinder axis. The field keeps reducing and reaches negative value, and correspondingly the magnetization of nanowire starts saturating in $-z$-direction.

For soft magnetic nanowires, there are two basic reversal modes depending on their thickness, which are known as the vortex wall mode and transverse wall mode. If the ferromagnetic nanowires are thin enough, nanowires can be approximated as two dimensional and the transverse wall mode can be performed. For our nickle nanowire with diameter 200 nm, it is a three dimensional structure and reversal process is in the vortex wall mode. As we can see, vortices start nucleating at the end of the wire and propagate along the wire axis. The reason why the domain formation starts at the end is that the demagnetizing

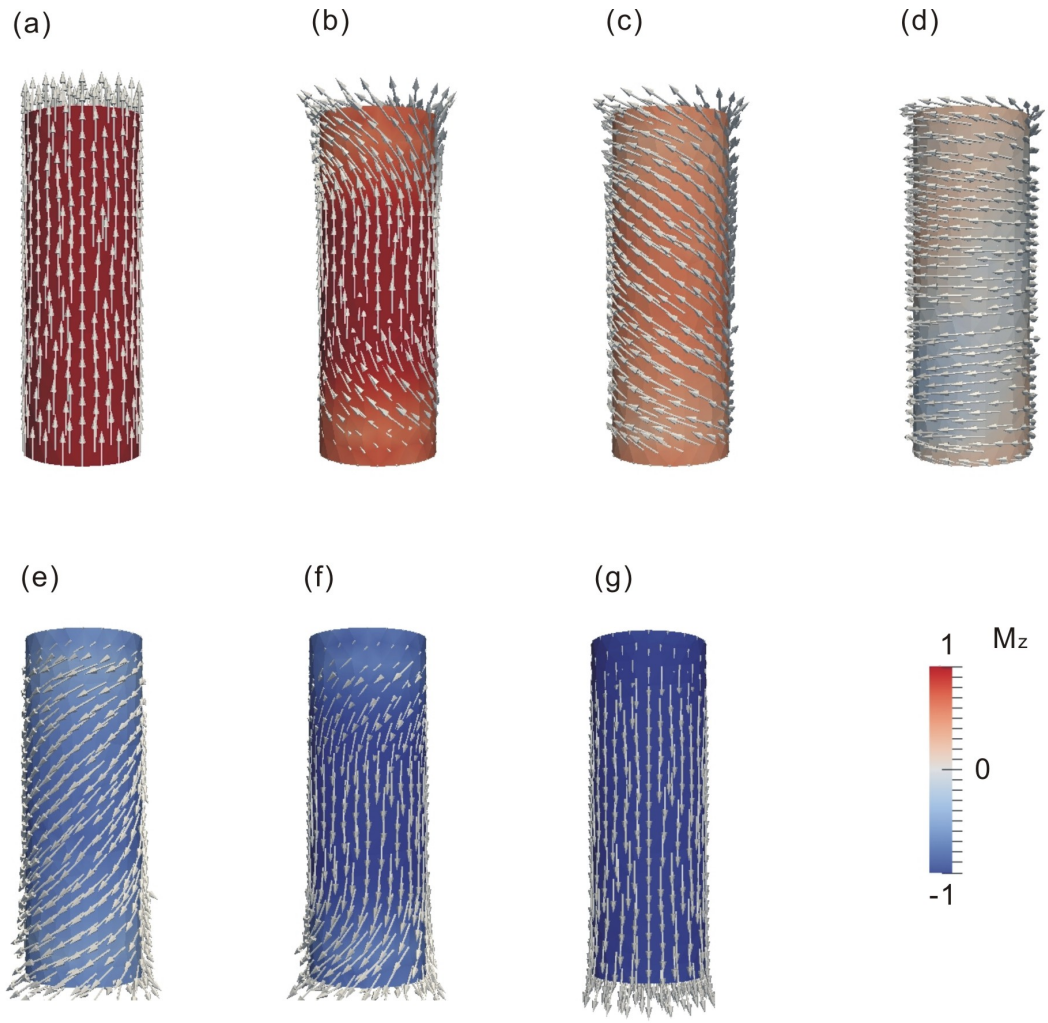

Figure 4.3: Magnetic reversal process. Simulation starts from saturation state (a), $M_z = 1$. External magnetic field is gradually reduced to 0, shown in (d), and reversed to the opposite direction to saturation state (b), $M_z = 1$. The color legend on the right bottom corner represents the projection of magnetization along z-axis.

field has its strongest value there. Gradually, the magnetic moments circle around the easy axis from the end to center. Vortices are formed on the cross sections with vortex cores in the center of the cylinder. As the external magnetic field reduce to 0, relaxation or reversal process with saturated initial state have vortex cores formed in the center of the cylinder, while vortices are also formed on the cylinder ruled surface when relaxation starts with random initialization due to large thickness. We can see that the initial magnetization affects magnetization of equilibrium status.

The domain formation within 200-nm-diameter nanowire minimizes the demagnetizing field outside of nanowire which leads to small magnetostatic energy. If the cross section area is decreased to 20 nm, the remanent state of nickel nanowire will be quasi single domain and initial magnetization does not affect the final state. The size of nanowire dramatically influences the competition between magnetostatic energy and exchange energy. Since only 200 nm is synthesized here, we will focus on the investigation on 200-nm-nickel nanowires.

The simulation on nanowire reversal provides us the hysteresis information of our 200 nm nickel nanowires. An external field is applied in the reversed order. The large magnetic field along $-z$-axis is applied at the beginning, increased to 0, and then reaches to the large value of the opposite direction which magnetizes the nanowire to saturation. The complete hysteresis information is obtained by reversing this process, starting with an external field from +z direction. Figure 4.4 plots the magnetization projection on z-axis over the external magnetic field. The plotted hysteresis curve is not a loop, but two overlapped lines. The lines go through the origin which means the magnetization along z-axis is 0 when the external magnetic field is removed. According to the simulation result, we can predict that our nickel nanowires cannot keep the desired pattern such as one-dimension chain or T-junction when the external magnetic field is removed. In order to perform the alignment, the external magnetic field has to be present until the nanowire solution completely evaporates.

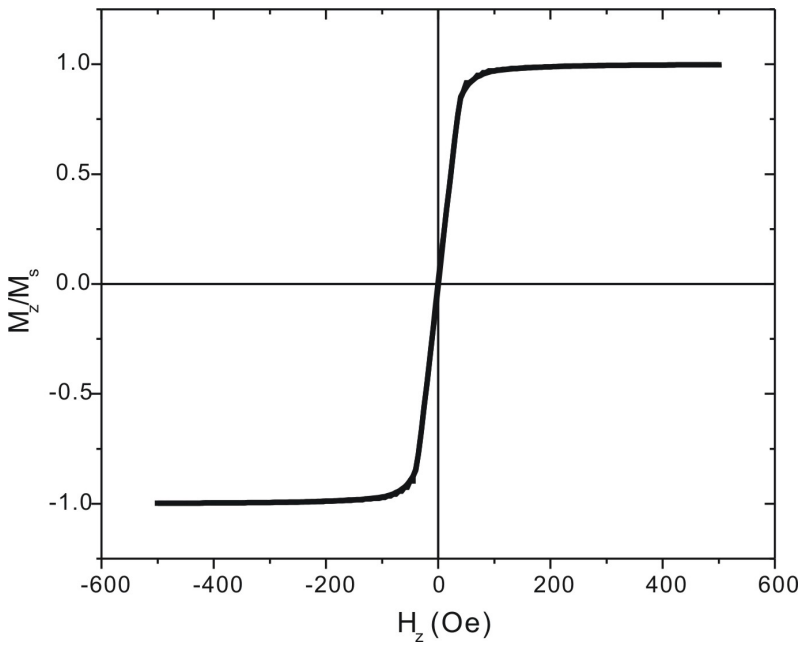

Figure 4.4: Hysteresis plot of nickel nanowire with 200 nm diameter. The plotted curve above is actually two overlapped lines that all go though origin point (0, 0).

The magnetic properties of 200 nm diameter nickel nanowire are obtained from previous simulation results. The relaxation processions and the non-hysteresis property show that the demagnetizing field outside the nanowire on z-direction is nearly 0 when no external magnetic field is applied. In order to align the wires in desired order, we have to keep the external field present until nanowire solution dries out, which will then indicate the fabricated nanowires will need sustainable external field during the alignment.

4.3 Nanowire Synthesis

The electrodeposition method is used for preparation of the ferromagnetic nanowire and multisegment nanowire is reported [66]. In this chapter, 200 nm nickel nanowires are prepared using electrodeposition method.

Commercially available Whatman Anodisc porous alumina has been widely used in recent nanoscale research, such as templates in nanowire fabrication through electrodeposition. This material has a precise, nondeformable honeycomb pore structure with no lateral crossovers. Three nominal pore sizes, 20, 100, and 200 nm, can be purchased from Whatman company. The Anopore porous alumina membranes are manufactured electrochemically [67]. The ideal membranes consist of a densely packed regular, hexagonal-shaped cells with pores in the cell center. Because the thickness of the membranes is about 60 μm, it is difficult to handle the membranes if they are immersed in aqueous solution without any support. A work electrode for electrodeposition, from which all of the nanorod growths inside the template, are rooted [68]. As a physical support and work electrode, an Ag layer needs to be coated on one side of the membranes.

A three-electrode setup is used here. The reference electrode is Ag/AgCl. The counter electrode is Pt. A layer of Ag deposited on the back side of the membrane serves as the working electrode. Electrical contact to the Ag is made using a silver plate, which the Ag

side of the membrane sits on.

Each membrane pore is first galvanostatically filled with about 20 μm of Ag. Then, Au is deposited in a chronocoulometry setup using potassium aurocyanide ($KAu(CU)_2$). The deposition rate of Au in alumina pores is experimentally determined to be 2.25 mC/nm. For the Nickel part, it is deposited in chronocoulometry setup as well. The plating solution is purchased commercial product by Technic Inc.. The deposition rate of Ni is 3.37 mC/nm in the alumina membranes. The last deposition is Ag, which is the same as the first layer Au deposition.

Surprisingly, the sizes and shapes of the nickel nanowires obtained by etching alumina membranes with nominal pore sizes of 20 nm and 100 nm are similar to those obtained by etching alumina membranes with a pore size 200 nm. Since the nominal pore size shows 20 nm, we expect the diameter to be much smaller. In Xiao's paper [68], it answers why 200 nm nanowires are obtained. Both the top and bottom surfaces of a membrane with 100 nm nominal pore size are imaged. The SEM image of the top surface of a membrane shows nominal size of 100 nm while the image of the bottom surface shows a totally different pore size of 200 nm. Cross-section images also shows the pore size of 200 nm even for membranes with a nominal pore size of $\sim$20 nm [68]. It shows that the 20 nm and 100 nm diameter pore sizes are defined by thin network layers, beneath which are pores of 200 nm. For the Whatman membrane, there are two layers: a porous alumina support layer and an active layer. The support layers have the nominal pore size of 200 nm for all three types, while the active layers contains smaller size pores. The pore size claimed by the company is actually the pore size of active layers. In some applications, such as filters, the hole size of the active layer determines what species can pass. For applications in nanoscale research, such as metal nanowire growth by electrodeposition, the pores in alumina support layer is useful. Here we will only investigate the aligning effect of 200 nm diameter nickel nanowires.

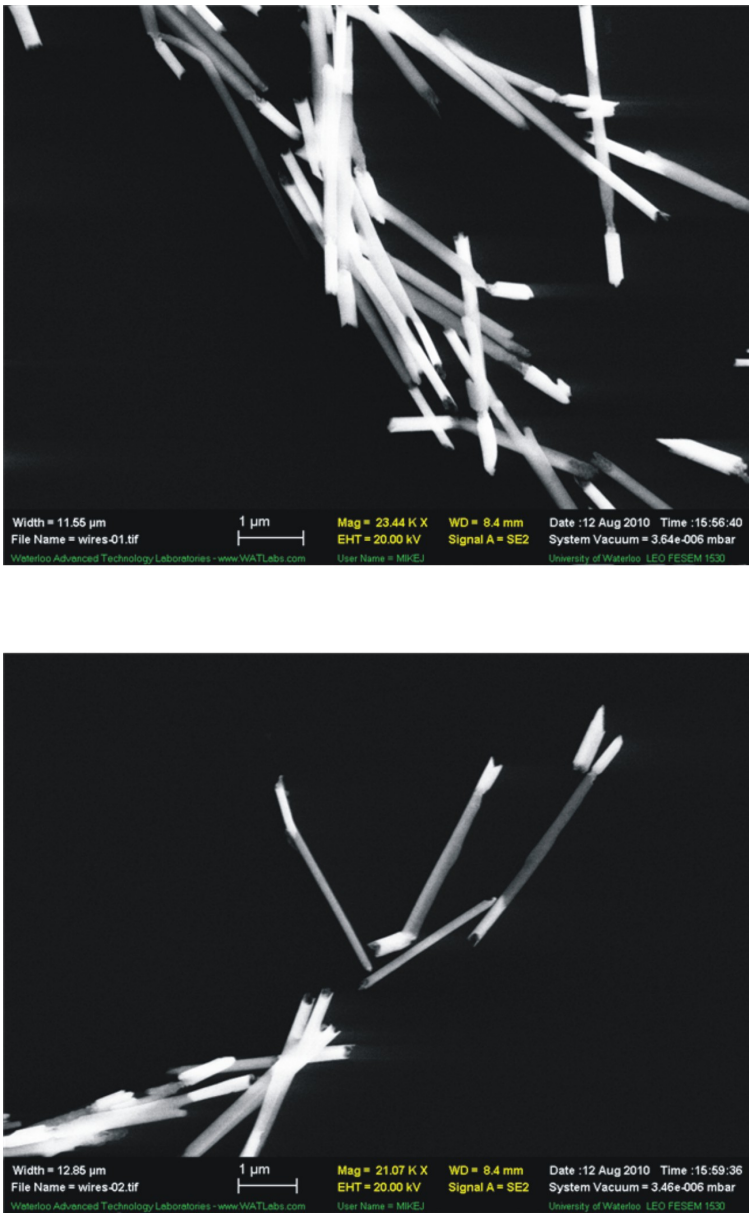

Figure 4.5: Scanning electron micrograph of Au-Ni-Au nanowires. The nanowires consist of Ni segment about 3 μm in the center and two Au caps at the end about 1 μm each.

When the electrodeposition is complete, the alumina membrane containing metal wires is removed from the electrochemical setup. The deposited Ag on the back side can be etched using a solution of 0.3 M nitric acid. The Ag etchant also etches Ni but not Au, thus keeping Au caps at the two ends are necessary to protect Ni segment. The membrane is immersed in the nitric acid for 10 minutes and the process can be repeated if necessary. During Ag removal, nanowires are trapped within the alumina membrane and sealed by Au at the ends. The next step is removing alumina membrane using 3 M sodium hydroxide (NaOH) which can release the nanowires into the water. Centrifugation after alumina membrane fully dissolves will separate nanowires from solution. Then replace NaOH with ethanol and repeat it for 10 times, so the final solvent used for storage of the wires is ethanol.

For the alignment, the diameter is fixed at 200 nm while we don't have specific requirements on the length of nanowires. Here, the nanowires with Au caps approximately 1 μm and Ni segment approximately 3 μm were fabricated. The Scanning Electron Microscopy (SEM) images are shown in Figure 4.5. In some cases, the Au caps are missing from the ends, which they have fallen off in the solution. One hypothesis is that some Au caps adjoin with the Ag layer on the back and fell off during etching.

4.4 Two-Dimensional Alignment

Electrostatic [69] and mangetic assembly [70, 71, 72] methods of metal nanowires have been studied preciously. Two techniques mainly used for self-assembly are free alignments in fluids and trapping. In magnetic assembly, free alignment in fluid typically includes the a droplet of a fluid containing magnetic nanowires; manipulation can be achieved by applying magnetic field (rotating or static). Trapping traditionally involves the addition of patterned ferromagnetic pads on the substrate, where the magnetic interaction between magnetic

nanowires and the ferromangetic pads attracts wires to be aligned [72]. Magnetic alignment is reported as a facile technique for assembling nanowires into two hierarchical structures. For the alignment of cross-junctions and T-junctions in this chapter, a sequential alignment technique on unpatterned substrates under the external magnetic field is used.

With the appropriate applied external magnetic field, two-dimension alignment requires two steps. The alignments are all carried on a glass slide which is cleaned using an isopropanol and ethanol rinse. The first deposition will create one-dimensional chains. In second alignments, deposited one-dimensional chains behave as ferromagnetic electrodes for subsequent nanowire alignments. Then the cross-junctions and T-junctions will be conducted on glass slides. Once a 5 μL droplet containing the nanowire has been placed on the substrate, then apply an external field. The external magnetic field is present until the solvent has fully evaporated in the air. The external field is generated by two bar magnets which are aligned parallel with a 7.5 mm gap in between where the droplet is placed. The field strength of a single bar magnet is measured to be 500 G at 1 cm from the magnet surface, and 1000 G at 0.5 cm from the magnet surface. After the droplet fully evaporates, we rotate the glass slide by 90°, keeping the two bar magnets aligned with 7.5 mm separation and placing the second 5 μL droplet.

There are several parameters that can be used within this work, such as dilution of wires, magnetic field strength, volume of the solution pipetted onto substrate, solvent viscosity, solvent evaporation rate, substrate wettability with solvent and so on. These factors play important roles on the nanowire travelling speed and travelling time, and strongly affect the alignment output. In order to disperse the nanowires well on the substrate, the substrate needs to be larger than the footprint of solvent droplet. A droplet of 5 μL is a reasonable small volume for our experiment. Ethanol and water are both tried as a solvent. Compared to water, ethanol has a relatively faster evaporation rate and better wettability on glass. So a 5 μL ethanol droplet evaporates much faster than water due to the larger droplet surface

and the faster evaporation rate. Although lower viscosity makes nanowires in ethanol have faster travelling speed than in water, the overall travel distance in ethanol is shorter than in water due to significant shorter travelling time. Water as solution is useful for investigation of alignment dynamics but long travelling time leads to large aggregation of nanowires at the edge under the magnetic field generated by our bar magnets. So, ethanol is used as solvent. In order to disperse nanowires well on the substrate and perform best alignment results, different nanowire concentrations of the solution are tested. High concentration results in nanowire aggregation that increases the chain width and also length, while low concentration leads to alignment which has relatively narrow width and short length. A weaker magnetic field results in a slower travelling velocity towards the edges of the substrate, so the concentration can be kept high as long as the magnetic field strength is reduced.

The optical microscope images of first deposition are shown in Figure 4.6 (a) and (b). From the images, it is noted that the chains are composed by multiple nanowires. At the edges of the drying droplet, the chain increases in length. The reason for increasing chain length at the drying edge may be the large travelling velocity that drags the nanowires to the edge where nanowires are able to adequately interact and join. The second deposition is essentially a trapping technique. The one-dimension chains in the first deposition act as the ferromagnetic traps. The second droplet is placed on the spot where the first droplet fully dries. Figure 4.6 (c) and (d) shows the two-dimension alignment. cross- and T-junctions are formed. This result confirms the trapping ability of the one-dimension chain.

The lateral aggregations in the chains are apparent in Figure 4.6. It may be lead by the nonlinear magnetic interactions for sufficiently high dipole strengths and nanowire concentrations. Nanowire concentration, low viscosity solvent, and a large transitional force produced by strong applied magnetic field can also influence the aggregation [73]. The chains consist of 5$\sim$20 nanowires. Please note that chain length in (a) and (b) is

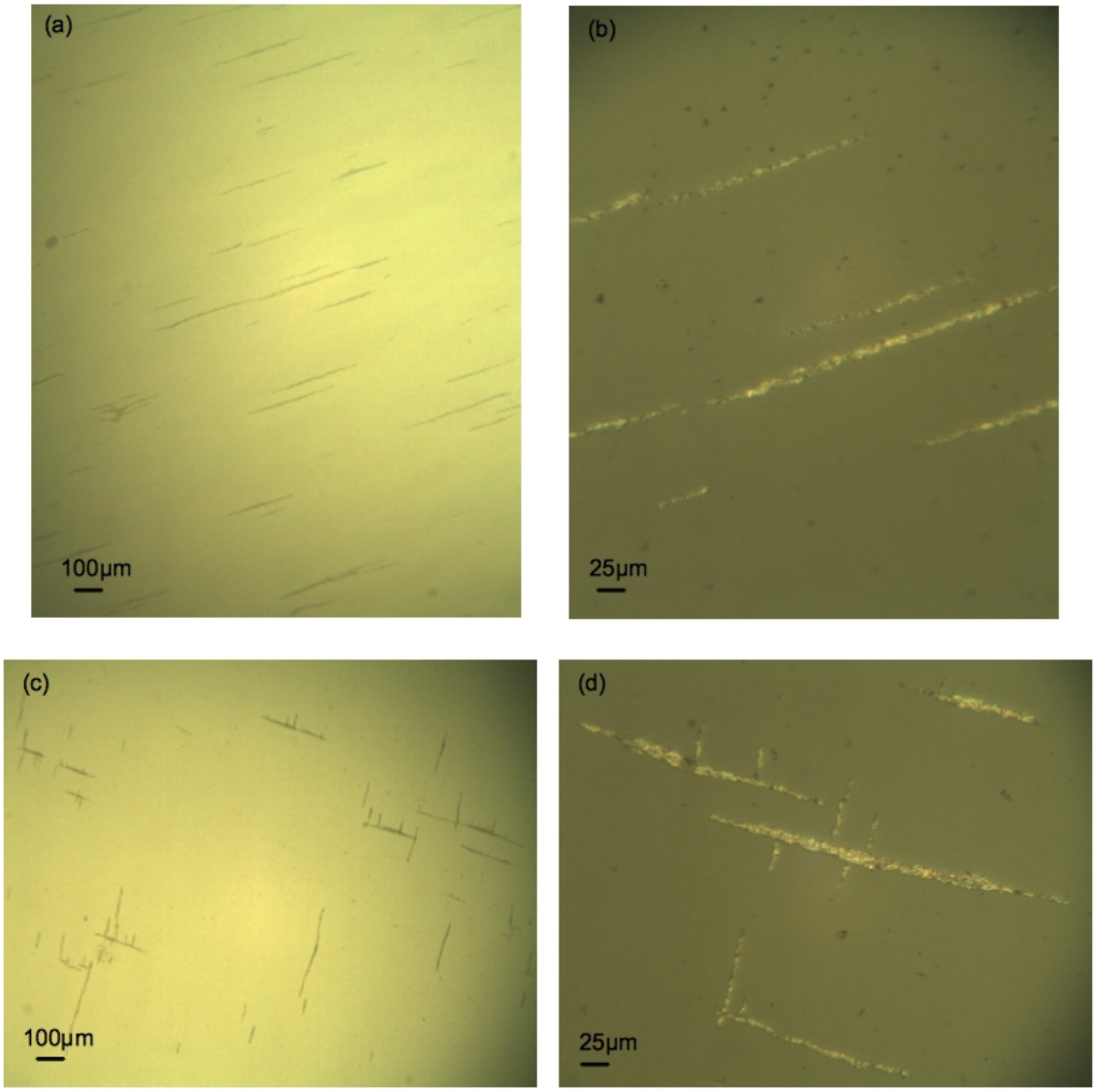

Figure 4.6: Optical microscope images. (a) and (b) shows the one-dimensional alignment. (c) and (d) show the two-dimensional alignment.

longer than the chaing length in (c) and (d), which are from different depositions. The possible reason for the visible length difference is that the surface area of the droplets on substrate of (a) is smaller than (b), which gives longer time for nanowires in (a) to travel.

The nanowires in second deposition form T-junctions by placing the second nanowire against the edges of a previously aligned nanowire. The cross-junctions occur in smaller proportion than T-junctions as the dipoles of the deposition will be separated by smaller distance in cross-junctions. The chains in Figure 4.6 have a tendency to align parallel with each other. The spacing between chains is caused by magnetic dipole repulsion. The nanowire concentration also plays a part in spacing.

In Figure 4.7(a), an external field is applied horizontally. The nanowires are aligned along the external field and fully magnetized along the cylinder axis. The nanowire can be treated as a magnetic dipole, and the dipole-dipole magnetic interaction is the dominant dragging force for the chain formation. After the solvent of the first deposition fully evaporates, the one-dimensional nanowire chains are fixed on the glass substrate and does not dissolve in the second droplet. Figure 4.7(b) shows the magnetization of nanowires during the second deposition where the external magnetic field is rotated by 90°. The external magnetic field is large enough to polarize the nanowires from first deposition along their hard axis, perpendicular to its cylindrical axis, allowing the nanowires to behave as ferromagnetic electrodes for the formation of T- and cross-junction [71]. The nanowires in the second droplet are magnetized along the nanowire cylinder axis. Through dipole-dipole interactions, the nanowires are dragged to align one-dimensionally like the first deposition and along the external magnetic field. Then, the two types of chains that are perpendicular with each other interact via dipole-dipole interaction as well.

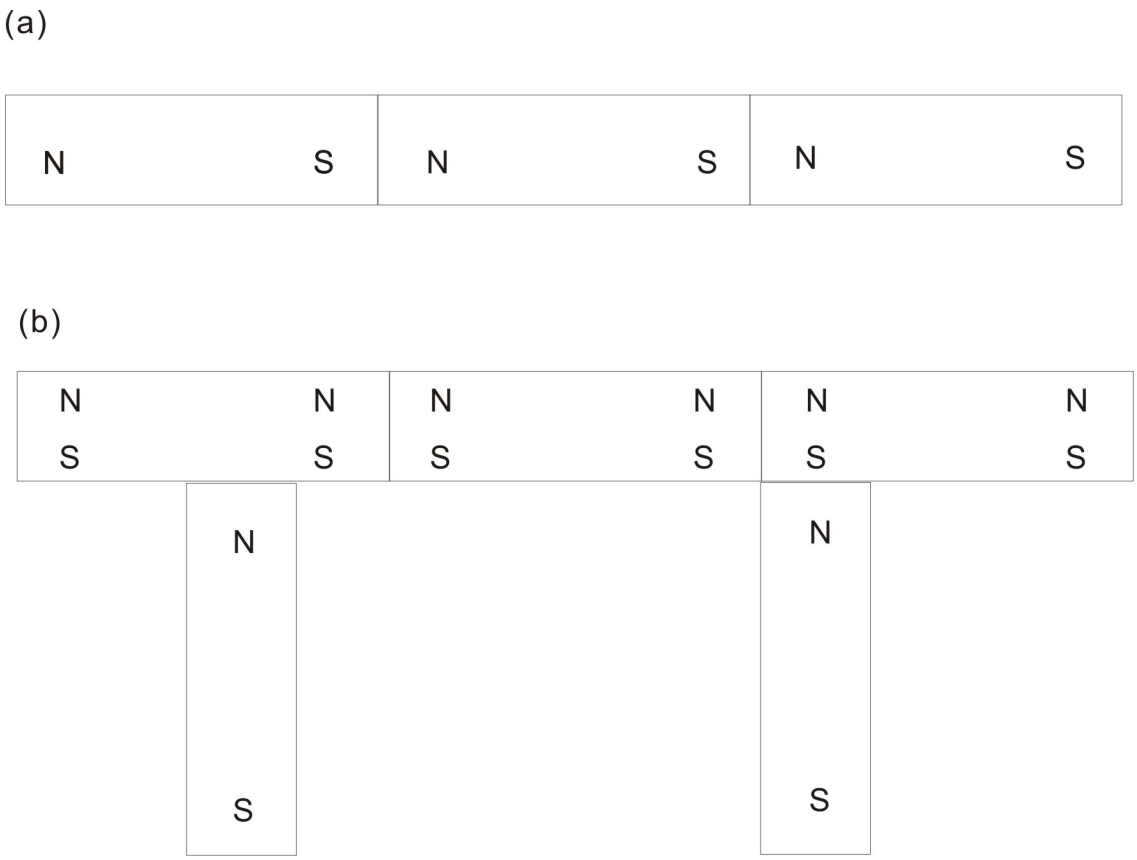

Figure 4.7: Alignment mechanism. (a) demonstrates the nanowire interactions in the one-dimensional alignment along external field. Upon the first deposition, nanowires in second deposition align perpendicularly to the chain by dipole-dipole interaction, shown in (b).

4.5 Three-Dimensional Alignment

In contemporary logic network design, three-dimensional computer architecture and technology is the research trend motivated by the saturation situation of Moore's Law. For conventional computers, planar and lithographic processing has largely been limited to a single layer of high quality semiconductor, so the microprocessor is two-dimensional on a single integrated circuit with all logic network elements of unit square size on it. Naturally, technologiests started exploring the third dimension for the 3D integration of chips. Here, the third dimension does not refer to the stacked two-dimensional integrated circuit layers but a dimension that relates to electrochemomechanical phenomena [74].

For conventional transistors, three-dimensional computer structure faces some challenges like over-heating and power dissipation. The magnetic logic devices which are non-volatile and theoretically no power dissipation provides the opportunity of constructing three-dimensional computer structures. Here we try to align a three-dimension magnetic nanowire network which has the potential to construct three-dimensional computing structures [20].

The two-dimensional alignment was achieved by two depositions with external magnetic field manipulation in the previous section. Here, we try to use the similar technique to develop the third dimension where an additional deposition is needed. The three-dimensional alignment faces lots of challenges. Above the aligned two-dimensional hierarchical nanowire structures on the glass slide, a third 5 μL droplet containing the nanowires is placed. As we know, the nanowires without an external magnetic field has vortex states inside and almost have no external stray field, and the external magnetic field is needed as a manipulation force which can align the nanowires and hold them in place until the solvent fully evaporates. During the third deposition, the external field will have to be kept present all the time, which can hold nanowires vertically against gravity. The droplet is three-dimensional. Once the droplet evaporates, the nanowires won't be able to stand vertically

and are going to fall down on the glass slide. Even with external field generated by the bar magnet, the third dimension alignment will still collapse as solvent evaporates and droplet surface lowers.

Next, we make attempts to maintain standing position of nanowires even when the external field is removed. Our goal is that the third dimension chains can be sustained in solvent after removal of the external magnetic field. Here, the solvent viscosity plays an important role. Within a high viscosity solvent, the random thermal motion can be reduced, and even motion caused by gravity could be eliminated. The viscosity needed to sustain the third dimension standing is unknown to us. There are two ways to find the desired viscosity range. One is to try various materials with different viscosities as solvents. The other is to use one material by manipulating its viscosity. The second option can provide continuous viscosity variations and give more flexibility, so one material was used in our three-dimensional alignment and the viscosity was controlled over temperature manipulation.

In previous sections, ethanol and water were tried as solvents. Ethanol evaporates fast and 5 ml ethanol can easily evaporate before the required experiment conditions are reached or before the three-dimensional alignment is observed. Once droplet is about to dry out, the surface tension will destroy the vertical alignment. Water is a good candidate for solvent which provides wide controllable viscosity and low evaporation rate. Water viscosity data obtained from Dortmund Data Bank [75] shows a wide range of viscosity with various temperatures.

Dynamic water viscosity data are plotted in Figure 4.8 with the viscosity as y-axis and temperature as x-axis. High viscosity can be achieved by lowering the temperature. Peltier cooler is a solid-state active heat pump which transfers heat from one side of the device to the other side with consumption of electrical power. The peltier cooler with small size and flat shape fits under the glass slide very well and we can use its cooling effect in our

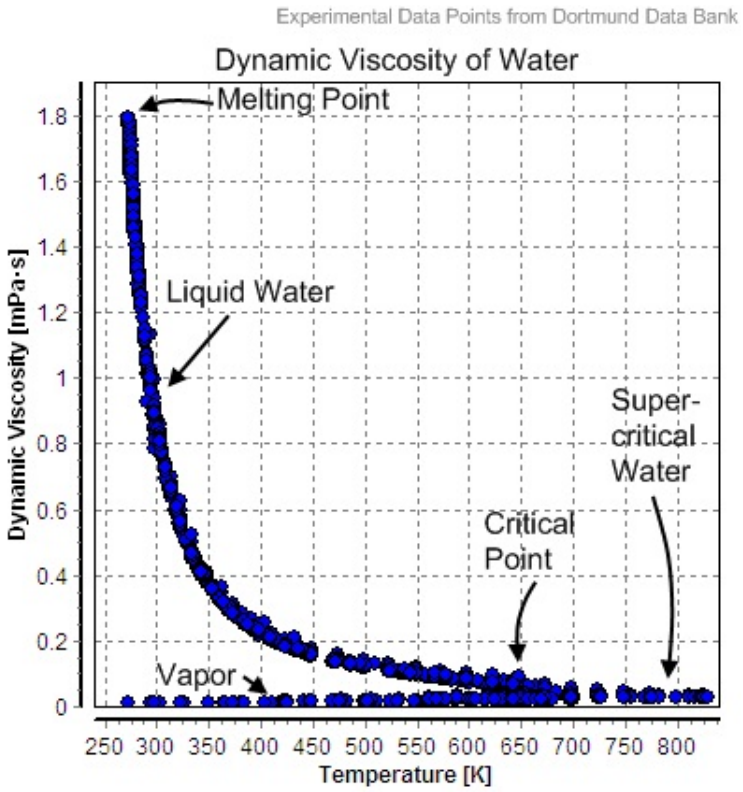

Figure 4.8: Dynamic viscosity of water (data obtained from DDB [75]). Dynamic viscosity is also called absolute viscosity. This plot lists viscosity of liquid water at different temperatures. In this section, only viscosity of liquid water is needed.

third alignment. At room temperature, water viscosity is not high enough to hold the third dimensional chain, and low viscosity is desired. Peltier cooler performance is a function of ambient temperatures. The typical maximum temperature difference between the hot side and cold side is 70°. To achieve low temperature, the hot side should maintain proper temperature. A cooling kit for heat dissipation is needed to prevent the hot side from overheating.

The main challenges faced by three-dimensional alignment are the observation of the third dimension. The precious planar nanowire alignments can be observed by optical

microscope or scanning electron microscope. For use of scanning electron microscope, the specimen chamber must be kept at high vacuum level, and the specimen should normally be completely dry, so scanning electron microscope is ruled out for alignment observation. For optical microscope use, the slight angle of the vertical external magnetic field will be able make the third dimension alignment observable. Under standard atmosphere, water solidifies at 0° and vertical nanowires will stay aligned. But the frost on the droplet surface prevents will create great difficulties of observation. Further development is needed for this part.

4.6 Summary

In this chapter, we studied the magnetic properties of nickel nanowires and their alignment. We investigated their magnetic remanent states and response to external magnetic field by means of micromagnetic simulations. Vortices were formed in the 200-nm-diameter nickel nanowires when no external field was applied, and the demagnetizing field returned to zero as well. In order to align the wires in the desired order. Deposited nanowires, which were aligned in an external field and fixed on a glass substrate, could serve as 'traps' for subsequent depositions of nickel nanowires. This trapping strategy gave the alignment the ability to form different two-dimensional structures, such as cross-junctions and T-junctions demonstrated in this thesis. Three-dimensional alignment was attempted as well. The same trapping concept was applied for the vertical alignment. Water was used as solvent in the third deposition to facilitate the vertical alignment of the nanowires. The high viscosity of the solvent was achieved by reducing the temperature.

Chapter 5

Conclusions and Future Work

5.1 Summary

Magnetic devices are highly attractive. They have the potential to achieve programmable and non-volatile logic functions, magnetic recording, and micromagnetic and spintronics sensors.

In this thesis, I established geometrical stability criteria for S-shaped elements by performing micromagnetic simulations. The geometric parameters of S-shaped elements played an important role in stabilizing the desired logic functionality. The detailed micromagnetic analysis of geometrical parameter space was presented. The two appendages give the biasing effect which made the coercive field shift. This coercive field shift is the basis of S-shaped element logic functionality. Geometrical criteria, like the size and aspect ratio of the center rectangular prism and appendages, are critical for logic operation. The center rectangular prism with a maximum width of 125 nm and minimum length of 190 nm is a good choice that can suppress flux-closure magnetization patterns. Appendages with an area between 1000 and 2000 nm^2 and an aspect ratio of up to 5/3 offer the appropriate effect for coercive field biasing.

Devices constructed by magnetic nanowires may have a wide spectrum of applications in the future. In order to build ordered structures, magnetic fields were used as an external stimulus force for nickel nanowire ordering. In this thesis, the magnetic behaviour of 200-nm-diameter nickel nanowires was investigated by micromagnetic simulations and by experiments. The vortex formation in the cylinder minimizes the overall energy, so that the demagnetizing field outside the nanowire was very small. This, in turn, prevents nanowires from self-ordering. Nickel nanowires with a diameter of 200 nm were synthesized by eletrodeposition into alumina pores. One-dimensional and two-dimensional alignment on a glass substrate was successfully performed and observed. Synthesized nanowires were diluted and stored in ethanol solvent for one-dimensional and two-dimensional alignment. First, a 5 μL droplet containing nanowires was placed onto a glass substrate in an external magnetic field. Then, a second 5 μL droplet was placed on top of the first one with a perpendicular external magnetic field present. Structures like T-junctions and cross-junctions were achieved. We attempted to add a vertical dimension on the two-dimensional structures by systematically varying the solvent viscosity. Viscosities of water and ethanol increase as the temperature drops. Hence, below a certain temperature, solvent viscosity should be large enough to hold the vertical alignment against gravity.

5.2 Future Work

The presented work on S-state reconfigurable magnetic logic devices was simulation-based. The next step is device fabrication. A large block of S-shaped elements with various geometrical parameters can be placed on a substrate with reasonable distance, and magnetic force microscope can be used to observe the magnetization of the elements. With S-state reconfigurable magnetic logic devices fabricated, the geometrical space identified by simulations can be experimentally verified.

Apart from S-state reconfigurable magnetic logic devices, nanostructures like ring structures, C-shaped structures, L-shaped structures, triangle structures and so on may be modified and configured as reconfigurable logic devices as well. These structures need to have a square-like hysteresis loop with abrupt switching behaviour and biasing parts that give coercive shifts. Consequently, their geometrical space could be investigated by simulations and ultimately experiments.

We attempted the three-dimensional alignment of Ni nanowires by varying the solvent viscosity. Observation difficulties and temperature control flexibility issues need to be solved for achieving alignment in the third dimension.

Bibliography

[1] R. R. Schaller, "Moore's law: past, present, and future," *IEEE Spectr.*, vol. 34, pp. 52–59, June 1997.

[2] O. Shacham, O. Azizi, M. Wachs, W. Qadeer, Z. Asgar, K. Kelley, J. Stevenson, S. Richardson, M. Horowitz, B. Lee, A. Solomatnikov, and A. Firoozshahian, "Rethinking digital design: Why design must change," *Micro, IEEE*, vol. 30, pp. 9 –24, nov.-dec. 2010.

[3] W. C. Black and B. Das, "Programmable logic using giant-magnetoresistance and spin-dependent tunneling devices (invited)," *J. Appl. Phys.*, vol. 87, pp. 6674–6679, 2000.

[4] A. Jaecklin, "A multiaperture magnetic control device," *Magnetics, IEEE Transactions on*, vol. 2, pp. 356 – 359, Sept. 1966.

[5] H. Gschwind, *Design of Digital Computers*. New York, NY: Springer Verlag, 1967.

[6] A. Imre, G. Csaba, L. Ji, A. Orlov, G. Bernstein, and W. Porod, "Majority logic gate for magnetic quantum-dot cellular automata," *Science*, vol. 311, pp. 205–208, Jan 13 2006.

[7] A. Imre, *Experimental study of nanomagnets for magnetic quantum dot cellular automata (mQCA) logic applications*. PhD thesis, University of Notre Dame, South Bend, IN, 2005.

[8] P. L. G. Csaba and W. Porod, "Power dissipation in nanomagnetic logic devices," pp. 346 – 348, aug. 2004.

[9] H. W. Schumacher, C. Chappert, R. C. Sousa, and P. P. Freitas, "Effective bit addressing times for precessional switching of magnetic memory cells," *Journal of Applied Physics*, vol. 97, no. 12, p. 123907, 2005.

[10] R. P. Cowburn, "Where have all the transistors gone?," *Science*, vol. 311, no. 5758, pp. 183–184, 2006.

[11] M. Meyyappan and M. K. Sunkara, *Inorganic Nanowires: Applications, Properties, and Characterization*. Boca Raton, FL, USA: CRC Press, 2010.

[12] Y. Cui, Z. Zhong, D. Wang, W. U. Wang, and C. Lieber, "High performance silicon nanowire field effect transistors," *Nano Lett.*, vol. 3, pp. 149–152, Nov 2003.

[13] H. Y. Cha, H. Wu, S. Chae, and M. G. Spencer, "Gallium nitride nanowire nonvolatile memory device," *J. Appl. Phys.*, vol. 100, no. 2, p. 024307, 2006.

[14] M. H. Huang, S. Mao, H. Feick, H. Yan, Y. Wu, H. Kind, E. Weber, R. Russo, and P. Yang, "Room-temperature ultraviolet nanowire nanolasers," *Science*, vol. 292, no. 5523, pp. 1897–1899, 2001.

[15] K. Kalantar-zadeh and B. Fry, *Magneitc Domains: The Analysis of Magnetic Microstructures*. Springer, 1998.

[16] S. Kato, S. Nigo, Y. Uno, T. Onisi, and G. Kido, "Voltage-induced insulator-metal transition at room temperature in an anodic porous alumina thin film," *Journal of Physics: Conference Series*, vol. 38, no. 1, p. 148, 2006.

[17] Y. G. Guo, L. J. Wan, C. F. Zhu, D. L. Yang, D. M. Chen, and C. L. Bai, "Ordered ni-cu nanowire array with enhanced coercivity," *Chem. Mater.*, vol. 15, pp. 664–667, 2003.

[18] D. A. Allwood, G. Xiong, M. D. Cooke, C. C. Faulkner, D. Atkinson, N. Vernier, and R. P. Cowburn, "Submicrometer ferromagnetic not gate and shift register," *Science*, vol. 296, no. 5575, pp. 2003–2006, 2002.

[19] V. Rodrigues, J. Bettini, P. C. Silva, and D. Ugarte, "Evidence for spontaneous spin-polarized transport in magnetic nanowires," *Phys. Rev. Lett.*, vol. 91, p. 096801, Aug 2003.

[20] S. N. Yanushkevich, V. P. Shmerko, and E. Sergey, *Logic Design of NanoICs*. Boca Raton, FL, USA: CRC Press, 2005.

[21] C. M. Hangarter, Y. Rheem, B. Yoo, E.-H. Yang, and N. V. Myung, "Hierarchical magnetic assembly of nanowires," *Nanotechnology*, vol. 18, no. 20, p. 205305, 2007.

[22] G. Snider and W. Robinett, "Crossbar demultiplexers for nanoelectronics based on n-hot codes," *Nanotechnology, IEEE Transactions on*, vol. 4, pp. 249 – 254, march 2005.

[23] A. Hubert and R. Schäfer, *Magneitc Domains: The Analysis of Magnetic Microstructures*. Springer, 1998.

[24] W. Heisenberg, "On the theory of ferromagnetism," *Z. Phys.*, vol. 49, p. 619, 1928.

[25] N. Spaldin, *Magnetic Materials: Fundamentals and Device Applications*. Cambridge University Press, 2003.

[26] R. Boardman, *Computer simulation studies of magnetic nanostructures*. Ph.D. thesis, University of Southampton, 2005.

[27] B. S. Oxford University Press, 1st edition ed., 2001.

[28] W. F. Brown, *Micromagnetics*. New York: Wiley, 1963.

[29] L. Landau and E. Liftshits, "On the theory of the dispersion of magnetic permeability in ferromagnetic bodies," *Phys. Zeitsch. der Sow.*, vol. 8, pp. 153–169, 1928.

[30] R. H. Engel-Herbert, *Micromagnetic study of self-organized magnetic nanostructures*. Ph.D. thesis, Humboldt-University, 2005.

[31] E. D. Dahlberg and J. G. Zhu, "Micromagnetic microscopy and modeling," *Physics Today*, vol. 18, pp. 34–40, 1995.

[32] G. Pelosi, "The finite-element method, part i: R. l. courant [historical corner]," *Antennas and Propagation Magazine, IEEE*, vol. 49, pp. 180–182, 2007.

[33] R. Engel-Herbert, T. Hesjedal, J. Mohanty, D. M. Schaadt, and K. H. Ploog, "Magnetization reversal in mnas films: Magnteic force microscopy, squid magnetometry, and micromagnetic simulations," *Phys. Rev. B*, vol. 73, p. 104441, 2006.

[34] R. Cowburn and M. Welland, "Room temperature magnetic quantum cellular automata,"

[35] G. Csaba and W. Porod, "Simulation of field-coupled computing architectures based on magnetic dot arrays," *J. Comput. Electr.*, vol. 1, pp. 87–91, 2002.

[36] S. Haque, M. Yamamoto, R. Nakatani, and Y. Endo, "Binary logic gates by ferromagnetic nanodots," *J. Magn. Magn. Mater.*, vol. 282, pp. 380–384, Nov 1 2004.

[37] L. Gross, R. R. Schlittler, G. Meyer, and R. Allenspach, "Magnetologic devices fabricated by nanostencil lithography," *Nanotechnology*, vol. 21, p. 325301, Aug 13 2010.

[38] A. Ney, C. Pampuch, R. Koch, and K. Ploog, "Programmable computing with a single magnetoresistive element," *Nature*, vol. 425, pp. 485–487, Oct 2 2003.

[39] B. Behin-Aein, D. Datta, S. Salahuddin, and S. Datta, "Proposal for an all-spin logic device with built-in memory," *Nat. Nanotechnol.*, vol. 5, pp. 266–270, Apr 2010.

[40] G. Prenat, B. Dieny, W. Guo, M. El Baraji, V. Javerliac, and J.-P. Nozieres, "Beyond MRAM, CMOS/MTJ integration for logic components," *Magnetics, IEEE Transactions on*, vol. 45, pp. 3400 –3405, oct. 2009.

[41] H. D. C. David R. Bennion and D. Nitzan, *Digital magnetic logic.* New York, USA: McGraw-Hill, 1969.

[42] B. Behin-Aein, S. Salahuddin, and S. Datta, "Switching Energy of Ferromagnetic Logic Bits," *IEEE Trans. Nanotechnol.*, vol. 8, pp. 505–514, Jul 2009.

[43] L. Hu and T. Hesjedal *unpublished*, 2011.

[44] S. Haque, M. Yamamoto, R. Nakatani, and Y. Endo, "Magnetic logic gate for binary computing," *Sci. Technol. Adv. Mater.*, vol. 5, pp. 79–82, Jan-Mar 2004.

[45] S. Haque, M. Yamamoto, R. Nakatani, and Y. Endo, "Binary logic gates by ferromagnetic nanodots," *J. Magn. Magn. Mater.*, vol. 282, pp. 380–384, Nov 1 2004.

[46] C. Pampuch, A. Das, A. Ney, L. Daweritz, R. Koch, and K. Ploog, "Magnetologic with alpha-MnAs thin films," *Phys. Rev. Lett.*, vol. 91, p. 147203, Oct 3 2003.

[47] T. Hesjedal and T.Phung, "Magnetic logic element based on an s-shaped permalloy structure," *Appl. Phys. Lett.*, vol. 96, p. 072501, 2010.

[48] J. Daughton, "Magnetoresistive memory technology," *Thin Solid Films*, vol. 216, pp. 162–168, Aug 1992.

[49] S. S. P. Parkin, K. P. Roche, M. G. Samant, P. M. Rice, R. B. Beyers, R. E. Scheuerlein, E. J. OSullivan, S. L. Brown, J. Bucchigano, D. W. Abraham, Y. Lu, M. Rooks, P. L. Trouilloud, R. A. Wanner, and W. J. Gallagher, "Exchange-biased magnetic tunnel junctions and application to nonvolatile magnetic random access memory (invited)," *Journal of Applied Physics*, vol. 85, pp. 5828 –5833, apr 1999.

[50] P. J. Strachan, *Time-resolved x-ray imaging of magnetic nanostructures driven by spin-transfer torque*. Ph.D. thesis, Stanford University, 2007.

[51] S. Parkin, "Giant Magnetoresistance In Magnetic Nanostructures," *Annu. Rev. Mater. Sci.*, vol. 25, pp. 357–388, 1995.

[52] J. S. Moodera, L. R. Kinder, T. M. Wong, and R. Meservey, "Large magnetoresistance at room temperature in ferromagnetic thin film tunnel junctions," *Phys. Rev. Lett.*, vol. 74, pp. 3273–3276, Apr 1995.

[53] T. M. Maffitt, J. K. DeBrosse, J. A. Gabric, E. T. Gow, M. C. Lamorey, J. S. Parenteau, D. R. Willmott, M. A. Wood, and W. J. Gallagher, "Design considerations for MRAM," *IBM Journal of Research and Development*, vol. 50, pp. 25 –39, jan. 2006.

[54] H. Kim, J. Lee, I. Baek, Y. Ha, J. Bae, S. Oh, S. Park, U.-I. Chung, N. Lee, H. Kang, and J. Moon, "Key factors to enhance the switching characteristics in submicron MRAM cells," *Magnetics, IEEE Transactions on*, vol. 40, pp. 2616 – 2618, july 2004.

[55] J. Deak, "Influence of pinned-layer dispersion on magnetic tunnel junction switching distributions," *Magnetics, IEEE Transactions on*, vol. 43, pp. 2821 –2823, june 2007.

[56] D. Allwood, N. Vernier, G. Xiong, M. Cooke, D. Atkinson, C. Faulkner, and R. Cowburn, "Shifted hysteresis loops from magnetic nanowires," *Appl. Phys. Lett.*, vol. 81, pp. 4005–4007, Nov 18 2002.

[57] M. R. Scheinfein, "LLG Micromagnetic Simulator." `http://llgmicro.home.mindspring.com`, 2010. [Online; accessed 24-December-2010].

[58] R. Hertel, "Thickness dependence of magnetization structures in thin Permalloy rectangles," *Z. Metallk.*, vol. 93, pp. 957–962, Oct 2002.

[59] G. Autès, J. Mathon, and A. Umerski, "Oscillatory behavior of tunnel magnetoresistance in a magnetic tunnel junction with varying magnetic layer thickness," *Phys. Rev. B*, vol. 84, p. 134404, Oct 2011.

[60] M. Herrmann, S. McVitie, and J. Chapman, "Investigation of the influence of edge structure on the micromagnetic behavior of small magnetic elements," *J. Appl. Phys.*, vol. 87, pp. 2994–2999, Mar 15 2000.

[61] B. B. Maranville, R. D. McMichael, and D. W. Abraham, "Variation of thin film edge magnetic properties with patterning process conditions in ni[sub 80]fe[sub 20] stripes," *Applied Physics Letters*, vol. 90, no. 23, p. 232504, 2007.

[62] M. Zhu and R. D. McMichael, "Modification of edge mode dynamics by oxidation in ni[sub 80]fe[sub 20] thin film edges," *Journal of Applied Physics*, vol. 107, no. 10, p. 103908, 2010.

[63] R. D. McMichael and B. B. Maranville, "Edge saturation fields and dynamic edge modes in ideal and nonideal magnetic film edges," *Phys. Rev. B*, vol. 74, p. 024424, Jul 2006.

[64] M. Hosomi, H. Yamagishi, T. Yamamoto, K. Bessho, Y. Higo, K. Yamane, H. Yamada, M. Shoji, H. Hachino, C. Fukumoto, H. Nagao, and H. Kano, "A novel nonvolatile

memory with spin torque transfer magnetization switching: Spin-RAM," in *IEEE Int. Elect. Devices Meeting*, International Electron Devices Meeting, pp. 473–476, 2005.

[65] K. Nielsch, R. B. Wehrspohn, J. Barthel, J. Kirschner, U. Gosele, S. F. Fischer, and H. Kronmuller, "Hexagonally ordered 100 nm period nickel nanowire arrays," *Applied Physics Letters*, vol. 79, no. 9, pp. 1360–1362, 2001.

[66] B. R. Martin, D. J. Dermody, B. D. Reiss, M. Fang, L. A. Lyon, M. J. Natan, and T. E. Mallouk, "Orthogonal self-assembly on colloidal gold-platinum nanorods," *Advanced Materials*, vol. 11, no. 12, pp. 1021–1025, 1999.

[67] "Anopore inorganic membranes (anodisc) @ONLINE."

[68] Z. L. Xiao, C. Y. Han, U. Welp, H. H. Wang, W. K. Kwok, G. A. Willing, J. M. Hiller, R. E. Cook, D. J. Miller, and G. W. Crabtree, "Fabrication of alumina nanotubes and nanowires by etching porous alumina membranes," *Nano Letters*, vol. 2, no. 11, pp. 1293–1297, 2002.

[69] P. A. Smith, C. D. Nordquist, T. N. Jackson, T. S. Mayer, B. R. Martin, J. Mbindyo, and T. E. Mallouk, "Electric-field assisted assembly and alignment of metallic nanowires," *Applied Physics Letters*, vol. 77, no. 9, pp. 1399–1401, 2000.

[70] M. Tanase, L. A. Bauer, A. Hultgren, D. M. Silevitch, L. Sun, D. H. Reich, P. C. Searson, and G. J. Meyer, "Magnetic Alignment of Fluorescent Nanowires," *Nano Letters*, vol. 1, pp. 155–158, Mar. 2001.

[71] C. M. Hangarter and N. V. Myung, "Magnetic alignment of nanowires," *Chemistry of Materials*, vol. 17, no. 6, pp. 1320–1324, 2005.

[72] A. K. Bentley, J. S. Trethewey, A. B. Ellis, and W. C. Crone, "Magnetic manipulation of coppertin nanowires capped with nickel ends," *Nano Letters*, vol. 4, no. 3, pp. 487–490, 2004.

[73] S. Chikazumi and C. Graham. Oxford University Press, 2nd edition ed., 1997.

[74] S. N. Yanushkevich, "Logic design of computational nanostructure," *J. Computational and Theoretical Nanoscience*, vol. 4, no. 3, pp. 467–481, 2007.

[75] J. Gmehling, J. Rarey, and J. Menke, "Dortmund data bank, oldenburg." `http://www.ddbst.com/`, 2011.